ACS APPLIED MATERIALS & INTERFACES

Research Article

www.acsami.org

Synthesis, Mechanical Properties, and in Vitro Biocompatibility with Osteoblasts of Calcium Silicate–Reduced Graphene Oxide Composites

Mehdi Mehrali,[†,‡] Ehsan Moghaddam,[§] Seyed Farid Seyed Shirazi,[*,†] Saeid Baradaran,[∥] Mohammad Mehrali,[†] Sara Tahan Latibari,[†] Hendrik Simon Cornelis Metselaar,[*,†] Nahrizul Adib Kadri,[‡] Keivan Zandi,[§] and Noor Azuan Abu Osman[‡]

[†]Department of Mechanical Engineering and Center of advanced Material, University of Malaya, 50603, Kuala Lumpur, Malaysia

[‡]Department of Biomedical Engineering, Faculty of Engineering, University of Malaya, 50603 Kuala Lumpur, Malaysia

[§]Tropical Infectious Diseases Research and Education Centre (TIDREC), Department of Medical Microbiology, Faculty of Medicine, University of Malaya, 50603 Kuala Lumpur, Malaysia

[∥]Department of Engineering Design and Manufacture, Faculty of Engineering, University of Malaya, 50603 Kuala Lumpur, Malaysia

ABSTRACT: Calcium silicate ($CaSiO_3$, CS) ceramics are promising bioactive materials for bone tissue engineering, particularly for bone repair. However, the low toughness of CS limits its application in load-bearing conditions. Recent findings indicating the promising biocompatibility of graphene imply that graphene can be used as an additive to improve the mechanical properties of composites. Here, we report a simple method for the synthesis of calcium silicate/reduced graphene oxide (CS/rGO) composites using a hydrothermal approach followed by hot isostatic pressing (HIP). Adding rGO to pure CS increased the hardness of the material by ~40%, the elastic modulus by ~52%, and the fracture toughness by ~123%. Different toughening mechanisms were observed including crack bridging, crack branching, crack deflection, and rGO pull-out, thus increasing the resistance to crack propagation and leading to a considerable improvement in the fracture toughness of the composites. The formation of bone-like apatite on a range of CS/rGO composites with rGO weight percentages ranging from 0 to 1.5 has been investigated in simulated body fluid (SBF). The presence of a bone-like apatite layer on the composite surface after soaking in SBF was demonstrated by X-ray diffraction (XRD) and field emission scanning electron microscopy (FESEM). The biocompatibility of the CS/rGO composites was characterized using methyl thiazole tetrazolium (MTT) assays in vitro. The cell adhesion results showed that human osteoblast cells (hFOB) can adhere to and develop on the CS/rGO composites. In addition, the proliferation rate and alkaline phosphatase (ALP) activity of cells on the CS/rGO composites were improved compared with the pure CS ceramics. These results suggest that calcium silicate/reduced graphene oxide composites are promising materials for biomedical applications.

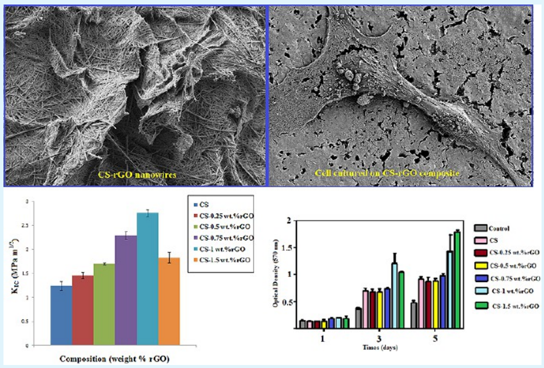

KEYWORDS: *calcium silicate, reduced graphene oxide, biocompatibility, bioactivity, mechanical properties*

1. INTRODUCTION

Graphene, a flat monolayer of carbon atoms in a two-dimensional (2D) honeycomb lattice with a high aspect ratio layer geometry and a very high specific surface area, has attracted tremendous attention in recent years due to its exceptional thermal, mechanical, and electrical properties.[1−4] Graphene sheets have been applied in various biotechnologies such as bacteria inhabitation,[5,6] biosensing,[7] drug delivery,[8] cellular imaging,[9] cancer targeting,[10] antiviral materials,[11] tissue engineering,[12−14] and so forth, due to its extremely large surface area, good biocompatibility, biostability, and ease of chemical functionalization. Much of the work on graphene composites has been focused on polymer matrix composites. The addition of graphene has resulted in the improvement of electrical and mechanical properties of the polymer matrix composites.[13,15,16] In recent years, there has been great interest in using graphene-based nanofillers, such as graphene oxide (GO), graphene nanoplatelets (GNPs), and reduced graphene oxide (rGO), to improve the mechanical performance of ceramics and bioceramics such as Si_3N_4,[17,18] zirconia/alumina composites,[19] Al_2O_3,[20] hydroxyapatite (HA),[21,22] and biphasic calcium phosphate composites.[23] All graphene-reinforced ceramic matrix composites were found to exhibit a decreased tendency to fracture, mainly due to crack bridging, crack

Received: November 19, 2013
Accepted: March 3, 2014
Published: March 3, 2014

deflection, crack tip shielding, and crack branching. Li et al.[24] synthesized nanohydroxyapatite on pristine and chitosan-functionalized graphene oxide (GO), which was densified using spark plasma sintering (SPS), to report on the effects of functionalized GO enhancing the cytocompatibility of a composite. Zhang et al.[22] prepared and characterized GNP/HA composites and reported the improvement of the mechanical properties, in vitro biocompatibility, good bone bonding ability, and promotion of the deposition of plate-like HA in a simulated body fluid (SBF) solution as compared to pure HA. In recent years, reduced graphene oxide has emerged as a competitively alternative material for graphene. Thermal annealing or chemical treatment can eliminate functional groups on GO to produce reduced graphene oxide (rGO).[25,26] Agarwal et al.[27] tested the biocompatibility of rGO with human fetal osteoblast (hFOB) cells, human oligodendroglia (HOG) cells, and rat pheochromocytoma (neuroendocrine cell, PC12) cells and found that rGO is biocompatible with all the cells tested.[27] Akhavan et al.[28] reported that the rGO sheets have no remarkable effects on genotoxicity in the human mesenchymal stem cells (hMSCs) . However, they found that interaction of rGO with stem cells and probably other biological systems such as organisms and tissues strongly depends on the lateral size of the sheets. Very recently, Liu et al.[21] found that the rGO reinforcement in HA for load-bearing orthopedic implants is compatible with hFOB cells with an increase in fracture toughness compared to pure HA. However, to the best of the authors' knowledge, there are no reports on the mechanical and biological properties by composites containing rGO and calcium silicate.

Calcium silicate ($CaSiO_3$, CS) is a novel biomaterial that enables excellent attachment and proliferation of osteoblast-like cells and promotes apatite formation, making it an attractive candidate biomaterial for hard tissue repair.[29−34] However, the insufficient strength and toughness of this material remain major hurdles that impede its application in load-bearing conditions.[35,36] The mechanical performance of CS can be improved by incorporating second-phase reinforcements such as ceramics,[36,37] metals,[38,39] and polymers.[40] However, few of the materials used in the preparation of CS composites combine favorable biocompatibility and adequate strength. The addition of biocompatible materials promotes the biological performance of CS. However, the mechanical strength is not usually improved enough to meet the requirements of high-load-bearing implants. On the other hand, researchers have shown that compared to conventional CS, calcium silicate nanowires possess a high aspect ratio, excellent bioactivity, and biological performance and are considered to be powerful reinforcing agents that greatly enhance the overall properties of nanocomposites.[41,42] Recently, hydrothermal synthesis was used to synthesize CS nanowires in the presence or absence of surfactant.[43,44] The hydrothermal method is a simple, low-cost, and nonpolluting method that can produce homogeneous CS nanowires. Moreover, hydrothermal treatment can effectively increase the crystallinity of the product.[41] It is difficult to increase the density of CS bioceramics by pressureless sintering methods, which lead to relative densities below 90%, bending strengths below 100 MPa, and fracture toughnesses (K_{IC}) below 1 MPam$^{1/2}$.[33,36] Therefore, the development of CS requires a suitable sintering technique, and the synthesis of CS-based composites may offer solutions that retain the high density and fine grain size of bulk materials. Among the most effective ceramic densification processes, hot isostatic pressing (HIP) permits such full densification with minimal grain growth. Furthermore, the application of this method to presintered samples allows for the densification of parts with highly complex shapes.

In this study, we first report a simple hydrothermal method to synthesize CS nanowires on reduced graphene oxide sheets. CS and CS/rGO composites are densified using HIP. The variation of the mechanical properties of CS/rGO composites with respect to the amount of rGO in the matrix has been systemically investigated. The effect of rGO content on the formation of HA on CS/rGO composites during soaking in a biomimetic system of simulated body fluid (SBF) were also evaluated. In addition, detailed in vitro experiments were performed such as cell adhesion, cell proliferation (MTT), and bone cell differentiation (ALP) experiments to explore the abilities of such materials to be successfully used in biomedical applications.

2. MATERIALS AND METHODS

2.1. Materials. Graphite flakes were purchased from Ashbury, Inc. Sulfuric acid (H_2SO_4, 98%), phosphoric acid (H_3PO_4, 98%), potassium permanganate ($KMnO_4$, 99.9%), hydrogen peroxide (H_2O_2, 30%), and hydrochloric acid (HCl, 37%) were purchased from Merck Company. Calcium nitrate tetrahydrate (Ca $(NO_3)_2{\cdot}4H_2O$) and sodium metasilicate nonahydrate ($Na_2SiO_3{\cdot}9H_2O$) were purchased from Sigma Aldrich Company. All aqueous solutions were prepared with double-distilled water (DI).

2-2. Synthesis of Graphene. Graphene oxide was synthesized from graphite using a simplified version of Hummers' method.[45] Graphene oxide was obtained by the oxidation of 3 g of graphite flakes with 120 mL of H_2SO_4 and the gradual addition of 18 g of $KMnO_4$. The solution was mixed using a magnetic stirrer, and the reaction took less than 5 min to complete. Nevertheless, to ensure complete oxidation of the graphite, the mixture was stirred for 3 days. During oxidation, the color of the mixture changed from dark purplish-green to dark brown. In the final step, the suspension was cooled and diluted with 350 mL of ice. Then, H_2O_2 (30%) was added until the gas evolution ceased to ensure that residual permanganate was reduced to soluble manganese ions. The graphene oxide was repeatedly washed with dilute 1 M HCl and deionized water until a pH of 4−5 was achieved. The product was separated from the mixture by centrifugation at 11 000 rpm.

2-3. Synthesis of CS−rGO Composites. The obtained GO (208.14 mg) was ultrasonically dispersed in 40 mL of distilled water for 2 h. In the first step, the GO solution was added dropwise to 20 mL of 0.2 M calcium nitrate tetrahydrate ($Ca(NO_3)_2{\cdot}4H_2O$) with stirring for 30 min, and the pH was adjusted to 11.5 with NaOH. Then, 20 mL of 0.2 M sodium metasilicate nonahydrate ($Na_2SiO_3{\cdot}9H_2O$) solution was added dropwise into the first solution, and the suspension was mechanically stirred for 1 h at room temperature to obtain a homogeneous suspension. In the final step, the suspension was transferred into a 60 mL Teflon-lined stainless-steel autoclave, heated to 200 °C for 24 h, and then naturally cooled to room temperature. Both the reduction of GO to rGO and the in situ synthesis of CS−rGO nanocomposites were expected to occur during the hydrothermal process. CS−rGO composite powders with different rGO contents (0, 0.25, 0.5, 0.75, 1, and 1.5 wt %) were produced. After the hydrothermal treatment, the suspension was filtered and washed several times by centrifugation and resuspension with distilled water. The resulting powders were dried at 100 °C for 24 h.

2.4. Hot Isostatic Pressing (HIP) Processing. The resulting powders were ball milled for 1 h and then uniaxially pressed into disks with diameters of 5 and 10 mm at a pressure of 250 MPa. These compacts were sintered by hot isostatic pressing (American Isostatic Presses, Inc.) for 1 h at 1150 °C in a high-purity argon atmosphere at 160 MPa. Heating and cooling rates were less than 5 °C/min to prevent the appearance of cracks due to differences in the thermal expansion coefficients of the phases that could form during sintering. Finally, the CS and CS/rGO composite compacts were ground using progressively finer silicon carbide papers (up to 1200 grit size), and then samples were polished to a mirror finish using diamond powders of various grades from 15 to 0.25 μm in an auto polisher (laboforce-3, Struers).

2.4. Characterization and Microstructures. Atomic force microscopy (AFM, Veeco Dimension AFM) in tapping mode was used to show the size of GO and rGO. The samples for the AFM imaging were prepared by drop casting a diluted suspension (0.05 mg/mL) onto a cleaned silicon substrate and dried at 50 °C for 1 day. The statistical analysis of the average lateral dimensions (ALDs) of GO and rGO were performed using the SPSS statistical software package version 19 (SPSS Institute, Chicago, IL), with the assistance of image analysis software. The microstructures of the synthesized powders (GO, rGO, CS, CS−rGO) were observed using a high-resolution FEI Quanta 200F field emission scanning electron microscope (FESEM). The CS−rGO composite interface was observed at near atomic scale under a transmission electron microscope (TEM, Zeiss Libra 120). The samples were prepared for TEM characterization by dispersing the powder in ethanol, placing it onto the micro grid, and letting the solvent evaporate. The X-ray diffraction (XRD) patterns of the powders and composites were obtained using an automated X-ray powder diffractometer (XRD, PANalytical's Empyrean) with monochromated Cu Kα radiation (λ = 1.54056 Å), operated at 45 kV and 40 mA with a step size of 0.026 deg and a scanning rate of 0.1 deg s^{-1} in the 2θ range of 20 to 60 deg. Energy dispersive X-ray analysis (EDAX) using the EDX-System (Hitachi, S-4800) instrument was attached to the FE-SEM instrument to investigate the elemental compositions of the samples. Fourier transform infrared (FTIR) analyses were carried out on a Perkin-Elmer System 2000 series spectrophotometer (U.S.A.) in the frequency range of 4000−400 cm^{-1} to identify the functional groups of the composites. Raman spectra were collected using a Renishaw Invia Raman Microscope with laser excitation at 514 nm. The Brunauer−Emmett−Teller specific surface areas of the samples were evaluated on the basis of nitrogen adsorption isotherms measured at 77 K using a BELSORP-max nitrogen adsorption apparatus (Japan, Inc.). The densities of sintered samples were measured by the Archimedes method. The values obtained are the average of five samples.

2.5. Evaluation of Mechanical Properties. Microhardness was measured using a Mitutoyo hardness tester (model AVK-C2, Mitutoyo, Kawasaki, Japan). A 1 kg Vickers load was applied to the polished samples for a loading time of 10 s. A total of 10 points were collected for each specimen. Nanoindentation experiments were conducted using a nanomechanical testing system (Micro materials Ltd., Wrexham, U.K.) with a Berkovich diamond tip with a radius of 20 nm and a controlled load of 100 mN with a dwell time of 10 s. The indentation velocity was 3 nm s^{-1}. At least 10 indentations were made to obtain an average value for each sample. The elastic modulus was calculated through nanoindentation. The reduced modulus (E_r) is taken from the nanoindentation data and is related to the sample's elastic modulus (E_s). The equations used to calculate the sample's elastic modulus (E_s) are as follows:

$$\frac{1-\nu_s^2}{E_s} = \frac{1}{E_r} - \frac{1-\nu_i^2}{E_i} \tag{1}$$

The elastic modulus (E_i) and Poisson's ratio (ν_i) of the indenter are 1140 GPa and 0.07, respectively. The Poisson ratio of the sample (ν_s) is taken to be 0.25.[46] The fracture toughness was then calculated from the equation suggested by Anstis:[47]

$$K_{IC} = 0.016\left(\frac{E}{H}\right)^{1/2}\left(\frac{P}{C^{3/2}}\right) \tag{2}$$

where K_{IC} is the indentation toughness (MPa m$^{1/2}$), 0.016 is the material-independent constant for a Vickers radial crack, E is the elastic modulus (GPa) determined from the nanoindentation experiments, H is the Vickers hardness (GPa), P is the indentation load (N), and C (m) is the half-length of the radial cracks on the surface after Vickers indentation.

2.6. Soaking in Simulated Body Fluid. The bioactivities of the fabricated CS/rGO composites were evaluated by examining the formation of bone-like apatite on the samples in simulated body fluid (SBF) solution, which was prepared according to the well-known Kokubo composition.[48] The as-sintered samples with a thickness of 3 mm and a diameter of 10 mm were soaked in SBF at 37 °C in a humidified atmosphere containing 5% CO_2 for 1, 3, 7, and 14 days at a surface-area-to-volume ratio of 0.1 cm^2/mL without refreshing the soaking medium. After various soaking periods, the samples were gently rinsed with deionized water to remove SBF and then dried in vacuum at 80 °C. The soaked samples were characterized by XRD. The surfaces of the soaked samples were observed by FESEM. At each SBF time point, the samples were removed, and the calcium (Ca) and phosphorus (P) ion concentrations in the SBF fluids were measured by inductively coupled plasma atomic emission spectroscopy (ICP-AES; Varian, U.S.A.). Changes in the solution pH were measured by a pH meter (Eutech pH 6+ pH/ORP meter kit (YO-15940-80)). As the SBF does not contain any Si before soaking, the dissolution ratio (S) of CS−rGO composites at different time points was calculated by the following equation:

$$S = (c_{Si}\nu_S)/m_{Si} \times 100 \tag{2a}$$

where c_{Si}, ν_S, and m_{Si} are the Si concentration in SBF (mg/mL), the volume of SBF (ml), and the Si content (mg) of the samples soaked in SBF, respectively.

2.7. Cell Culture. The hFOB 1.19 cell line derived from human osteoblasts was purchased from American Type Culture Collection (ATCC, Rockville, MD). Cells were maintained and propagated in DME/F-12 (HyClone, UT) cell culture medium supplemented with 10% fetal bovine serum (Gibco, NY), 100 U/ml penicillin, and 100 μg/mL streptomycin at 37 °C in a humidified atmosphere with 5% CO_2. The ability of the cells to attach and proliferate on the CS/rGO composites was examined by culturing the cells on composite discs. The CS/rGO composite discs, 5 mm in diameter and 2 mm thick, were sterilized by autoclaving at 121 °C for 30 min under a pressure of 15 atm. Composites were then washed by sterile phosphate-buffered saline (PBS) to remove all residues. In the next step,

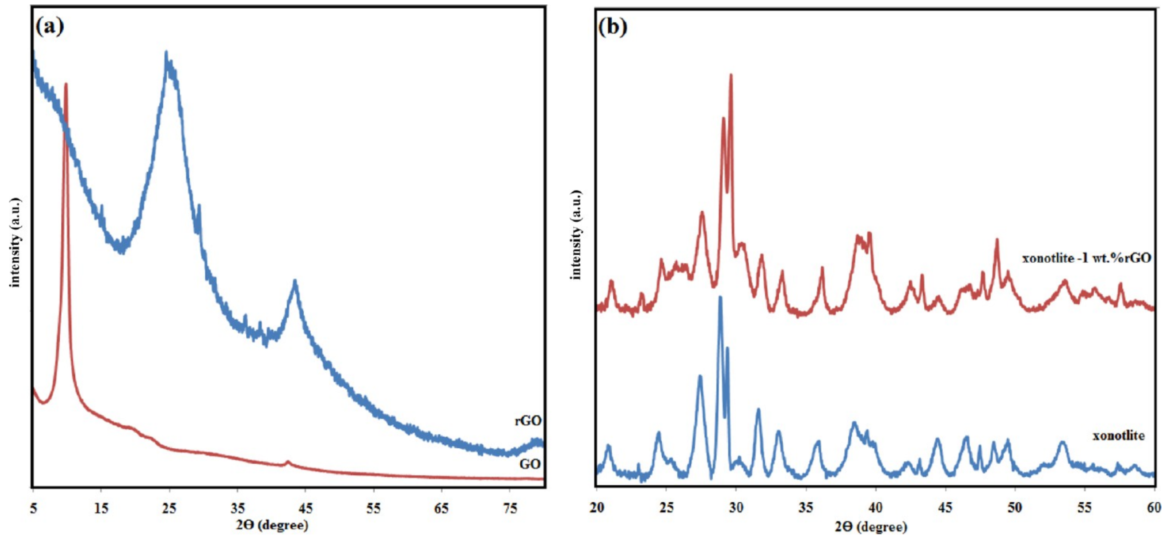

Figure 1. (a) XRD patterns of GO and rGO. (b) XRD patterns of pure Xonotlite and Xonotlite−1 wt % rGO composite.

the samples were washed with the cell culture medium prior to placement in a 96-well tissue culture plate (NUNC, Denmark). Cells were seeded at 1 × 10^4 cells/well in wells containing composite discs.

2.8. Cell Attachment and Proliferation Assay. The cells were seeded on the sterilized surfaces at 1 × 10^4 cells ml^{-1} in 96-well culture plates with 200 μL media in each well and cultured for 1, 3, and 5 days. The proliferation of the cells cultured on the sterilized pellets was analyzed using the methyl thiazole tetrazolium (MTT) assay. A 5 mg mL^{-1} MTT stock solution (Sigma, St. Louis, MO) was prepared by dissolving MTT in PBS, filtering the solution with a 0.2 μm filter, and storing at 4 °C. When the 96-well plates were removed from the incubator, 20 μL of MTT stock solution was added to each well. Cells were incubated for 4 h at 37 °C in an atmosphere of 100% humidity and 5% CO_2. After incubation, the MTT solution was removed and replaced with 100 μL of DMSO. At each time point (1, 3, and 5 days), the samples were removed to new 24-well tissue culture plates. After three washes with PBS solution, the cells were detached with trypsin/EDTA, stained with trypan blue, and the living cells were counted with a hemocytometer (Becton Dickinson, Germany). Dose−response curves were plotted using GraphPad Prism 5 (GraphPad Software, Inc., San Diego, CA). Three samples of each composite were tested, and each test was carried out in triplicate.

2.9. Cell Morphology. To observe the cells adhering to the sample surfaces after incubation for 1, 3, and 5 days using FESEM and confocal laser scanning microscopy, the cells were fixed on the specimen surfaces with 4% glutaraldehyde for 2 h at room temperature, followed by three washes in PBS (0.1 M) and dehydration with a series of graded ethanol/water solutions (40%, 50%, 60%, 70%, 80%, 90%, and 3 × 100%, respectively). Then, 0.5 mL of hexamethyldisilazane (HMDS) was added to each well to preserve the original cell morphology, and the test plates were kept in a fume hood to dry at room temperature.

2.10. Confocal Laser Scanning Microscopy. The specimens were washed with 1× PBS before staining with 100 μg/mL acridine orange (Sigma Aldrich) for 5 min at room temperature. Excess stain was removed by washing twice with 1× PBS for 10 min each. The stained cells were then analyzed using confocal microscopy (Leica TCS-SP5 II, Leica Microsystem, Mannheim, Germany), and the images were processed with Leica LAS AF software.

2.11. Alkaline Phosphatase Activity Assay. To assess alkaline phosphatase (ALP) activity, hFOB human osteoblast cells were seeded (3 × 103 cells/disc) onto the samples (Ø 5 × 2 mm) and incubated for 7 days. Quantitative ALP activity was measured by an assay based on the hydrolysis of *p*-nitrophenyl phosphate (*p*-NPP) to *p*-nitrophenol (*p*-NP). Cells were extracted from the samples and permeabilized using Triton X-100 (1 vol %) solution (Sigma, St. Louis, MO). The cell lysate from each sample was then used for the ALP assays. The absorbance was recorded at 405 nm using a M5 SpectraMax microplate reader (Molecular Devices, Sunnyvale, CA), and ALP activity was calculated from a standard curve after normalization to the total protein content. Data were expressed in nanomoles of *p*-nitrophenol produced per minute per microgram of protein. Five replicates were used, and each test was performed independently three times.

2.12. Statistical Analysis. All data are expressed as the mean ± standard deviation (SD) and were analyzed using a one-way analysis of variance (ANOVA) and a Tukey−Kramer post hoc test. $P < 0.05$ was considered statistically significant.

4. RESULTS AND DISCUSSION

4.1. Synthesis and Consolidation of CS/rGO Composites. The XRD spectrum of the GO in Figure 1a is similar to those in other reports.[49,50] The XRD pattern of GO shows an intense and sharp diffraction peak at $2\theta = 9.85°$, attributed to the (001) lattice plane corresponding to a *d*-spacing of 0.83 nm. This is consistent with the lamellar structure of GO. GO sheets can be reduced under hydrothermal conditions, resulting in the disappearance of this strong peak and the appearance of a very broad (002) peak and a very weak (100) peak at 2θ values of 24.53° and 43.45°, respectively, corresponding to *d*-spacings of 0.36 and 0.20 nm, respectively. This implies that the GO was reduced to rGO sheets due to the removal of functional groups from the GO after the hydrothermal process.[51,52] Figure 1b presents the XRD spectra of the products obtained after hydrothermal processing at 200 °C for 24 h in the absence and presence of rGO, which are dominated by the Xonotlite phase reflection peaks (JCPDS card no. 23-0125). The Xonotlite crystal is a calcium silicate-type hydrated calcium silicate. The

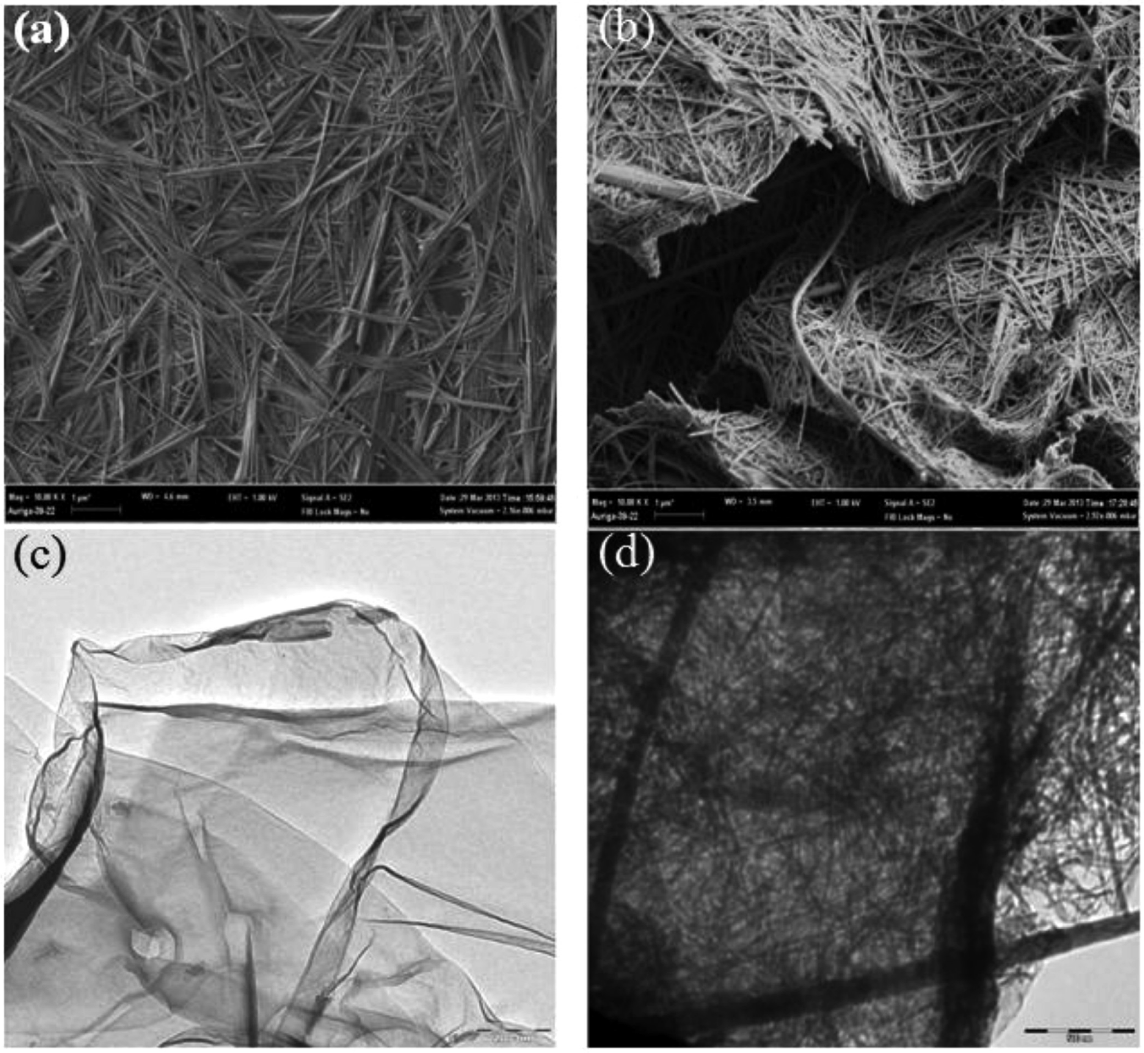

Figure 2. FESEM micrographs of pure Xonotlite (a), Xonotlite−1 wt % rGO composites (b) and TEM images of GO (c) and Xonotlite−rGO composites (d) synthesized via the hydrothermal technique.

XRD analysis further indicates that the main diffraction peaks of the Xonotlite phase with GO are similar to those of the pure Xonotlite phase. No other reflection peaks are observed, including (001) GO reflections, indicating the formation of a high purity Xonotlite phase and hydrothermal reduction of the GO to rGO. Moreover, no typical diffraction peaks of rGO are detected in the composites, which can be explained by the low diffraction intensity peak and the low amount of rGO.

In the absence of rGO, the Xonotlite phase appears as nanowires with approximate diameters of 10−30 nm and lengths of up to several micrometers, similar to the results reported by Kaili Lin et al.[53] As depicted in Figure 2a, no other morphologies are observed in the FESEM images. Figure 2b shows similar morphological features in the Xonotlite−rGO composites. The TEM observation presented in Figure 2c,d show that the rGO sheet is very thin, with few wrinkles and folds. Moreover, the rGO nanosheets are efficiently decorated with Xonotlite nanowires on both sides of the translucent sheets, as shown in Figure 2b,d.

AFM was used to analyze the lateral dimensions of the graphene oxide and reduced graphene oxide sheets, as shown in Figure 3. The as-prepared GO sheets with average lateral dimensions (ALDs) of 3.88 ± 0.99 μm are presented in Figure 3a,c. The pure rGO prepared by hydrothermal technique at 200 °C for 24 h resulted in partial fragmentation of the sheets and consequently smaller ALDs (2.37 ± 0.65 μm), as shown in Figure 3b,d for the hydrothermal rGO sheets.

To verify the formation of graphene oxide, reduced graphene, and Xonotlite nanowires in the absence and presence of rGO, the infrared spectra of the samples were measured and are compared in Figure 4. The FTIR spectrum presents all the characteristic bands for GO, including the appearance of the broad peak from 900 to 1200 cm^{-1} attributed to C−O stretching and the peak at 1370 cm^{-1}representing tertiary alcoholic C−OH bending. Other features include the stretching vibration of the sp^2 hybridized C═C bond at 1625 cm^{-1}, the C═O stretching vibration at 1720 cm^{-1}, and the common hydroxyl stretching around ~3430 cm^{-1}.[45,51] Figure 4 presents the FTIR spectrum of the rGO following hydrothermal reduction, including absorption peaks representing the C−O stretching vibrations of epoxy groups at 1050 cm^{-1} and the deformation of C−OH at ~1430 cm^{-1}. Moreover, the characteristic peaks of rGO nanosheets are usually recognized as the asymmetric stretching of CH_2 at 2920 cm^{-1} and the symmetric stretching of CH_2 at 2850 cm^{-1} at the edges/defects.[54] The FTIR spectrum of the pure Xonotlite sample

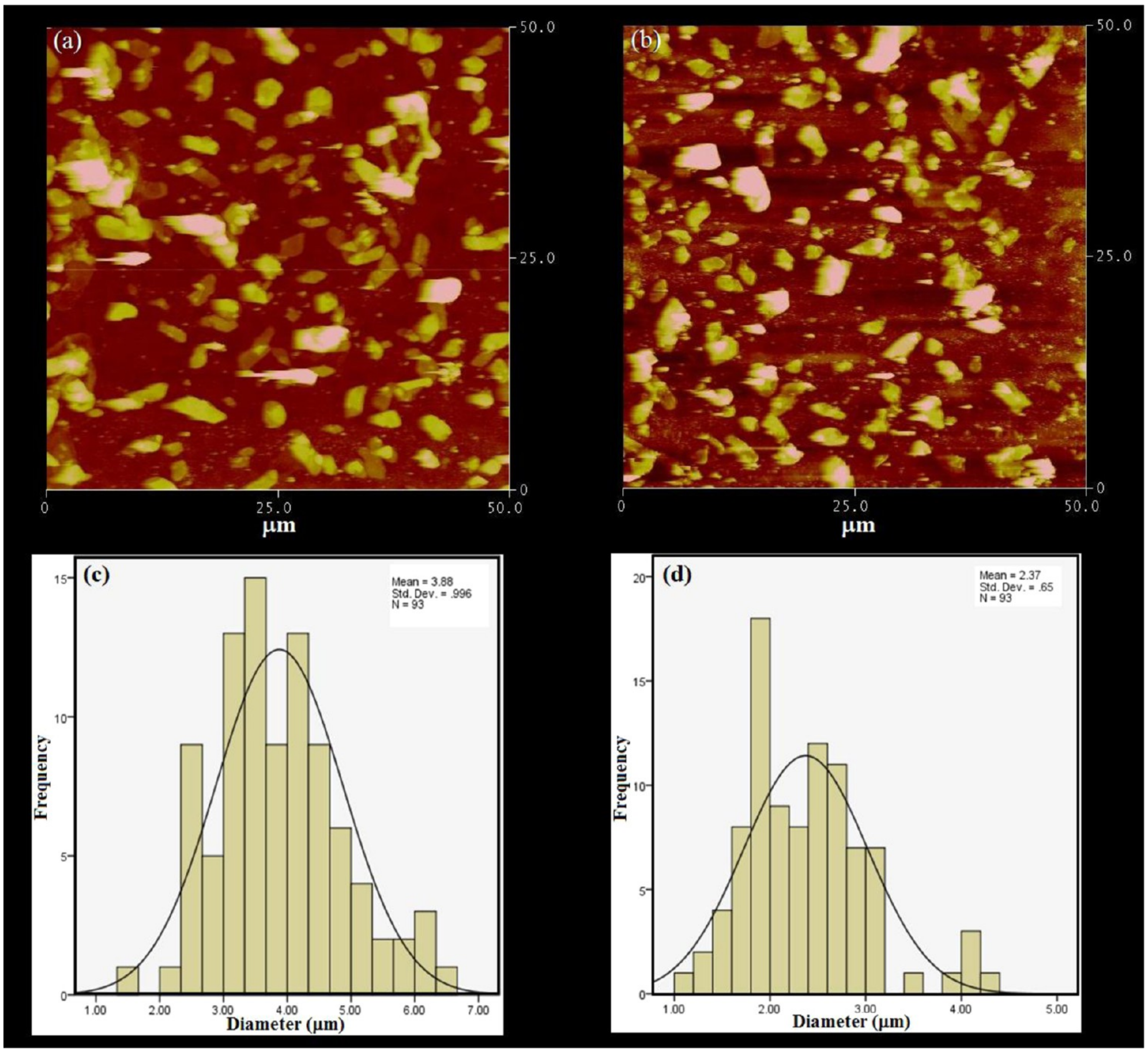

Figure 3. AFM images of the as-prepared GO sheets (a), pure rGO prepared by the hydrothermal technique at 200 °C for 24 h (b) and size distribution diagram of GO (c) and rGO (d).

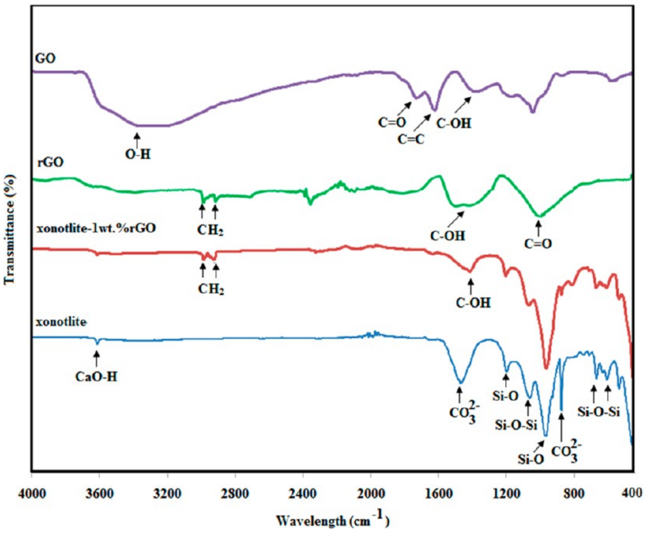

Figure 4. FTIR spectra of the GO, rGO, pure Xonotlite, and Xonotlite−1 wt % rGO composites.

shows a sharp spike at 3610 cm^{-1} due to the CaO−H stretching vibration, and its bending mode is observed at 630 cm^{-1}. The characteristic bands for the CO_3^{2-} group occur in the spectrum at 1470 cm^{-1} (ν_2, asymmetric stretch vibration) and at 875 (ν_2, out-of-plane bend vibration). Note that no carbonates are detected by XRD analysis, whereas CO_3^{2-} bands appear in the powder spectra. This may be due to contamination with CO_2 during powder preparations and drying. Generally, Xonotlite has a characteristic band at approximately 1200 cm^{-1}; this band is due to the Si−O stretching of vibrations in Q^3 sites (silicate tetrahedra link two silicate chains).[55] The bands at 1065 and 970 cm^{-1} can be attributed to the symmetric stretching modes of Si−O−Si and Si−O, respectively. The bands observed at 670 and 607 cm^{-1} are related to the Si−O−Si bending vibrations. The CS/rGO composite exhibits clear absorption bands resulting from the asymmetric stretching of CH_2 at 2920 cm^{-1} and the symmetric stretching of CH_2 at 2850 cm^{-1}, which are inherent to reduced graphene oxide. The peak at approximately 1430 cm^{-1} was attributed to the deformation of CO−H, and this band has been observed in pure rGO. The other absorption bands are attributed to the Xonotlite.

The structure, defect levels, and crystallinity of the reduced graphene oxide sheets in the composites were studied by further structural characterization using Raman spectroscopy.

For comparison purposes, the Raman spectrum of graphene oxide is also shown in Figure 5. The Raman spectrum of GO displayed a band at 1595 cm^{-1} named the "G band" and another band at 1360 cm^{-1} named the "D band". The G band represents the planar configuration of sp^2-bonded carbon that makes up graphene, and the D band is due to the breathing modes of six-atom rings and requires a defect for activation[1]. The Raman spectrum of the Xonotlite/rGO composite exhibits significant changes compared to the spectrum of GO. Both the G band and D band are shifted toward lower wave numbers of 1346 and 1593 cm^{-1}, respectively, and a 2D peak at approximately 2688 cm^{-1} (Figure 5) indicates an increase in the number of layers in rGO compared to GO. The intensity ratio of the D to G bands (I_D/I_G) is a measure of the degree of disorder and the average size of the sp^2 domains in graphene materials.[2] The I_D/I_G ratios for GO and Xonotlite/rGO composites were found to be 0.79 and 0.83, respectively, as shown in Figure 5. The increase in the I_D/I_G ratio after the hydrothermal reaction suggests that there the graphene lattice contains structural defects and that the reaction decreases the average size of the sp^2 domains.[56] This result is in agreement with that of the AFM observation mentioned above. As seen in Figure 5, the spectrum of the Xonotlite/rGO composite before sintering exhibits a single peak representing the Xonotlite phase at 1088 cm^{-1}, which can be attributed to the Si−O−Si asymmetric stretching mode (ν_{as}(Si−O−Si)).[57] Exposure to high temperature during sintering makes it necessary to test for the survival of the rGO structure in the final samples. The presence of G and 2D peaks in the CS/rGO composites indicates the survival of rGO after HIP processing. As shown in Figure 5, the I_D/I_G ratio of the bulk Xonotlite/rGO composite increased from 0.83 to 1.24 after HIP, demonstrating that the HIP process introduces structural defects into rGO. The intensity ratio of I_{2D}/I_G decreased, and the 2D peak became narrower, sharper, and shifted to higher wavenumbers compared with before sintering, indicating that rGO bonding may also occur during the HIP of the CS/rGO composites and that the number and thickness of layers may be increasing.[1,58] The broad peak at approximately 2940 cm^{-1} was assigned to the combination of the D and D′ bands (D + D′).[54] Thus, Raman spectroscopy demonstrates that the rGO structure is retained after HIP consolidation. Furthermore, two characteristic Raman peaks for the CS at 635 and 970 cm^{-1} were detected in CS/rGO composites after the HIP process and are attributed to the Si−O−Si bending vibration and the Si−O stretching vibration, respectively.[57,59]

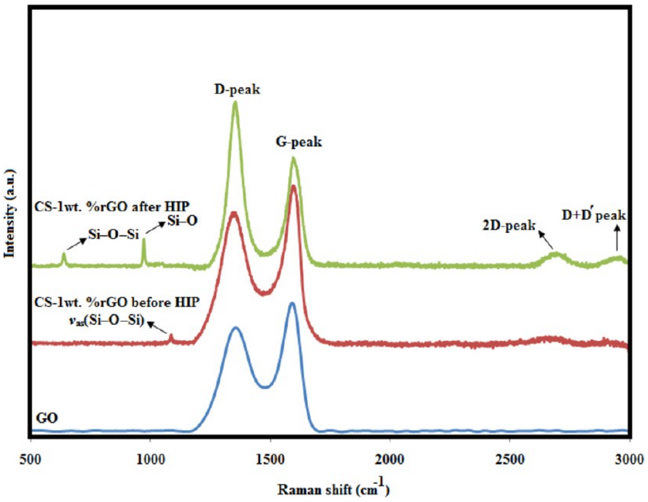

Figure 5. Raman spectra of GO and CS−1 wt % rGO composites before and after HIP.

To verify the phase after HIP, the samples were investigated by XRD, as shown in Figure 6. The peaks in all six patterns are indexed as $CaSiO_3$ (standard card no. JCPD 31-0300), which illustrates that the Xonotlite transformed to $CaSiO_3$ during HIP. XRD analysis confirmed that rGO and HIP processing did not induce the formation of any other phase. In the CS/rGO composites, it is difficult to detect the rGO by XRD due to its small content.

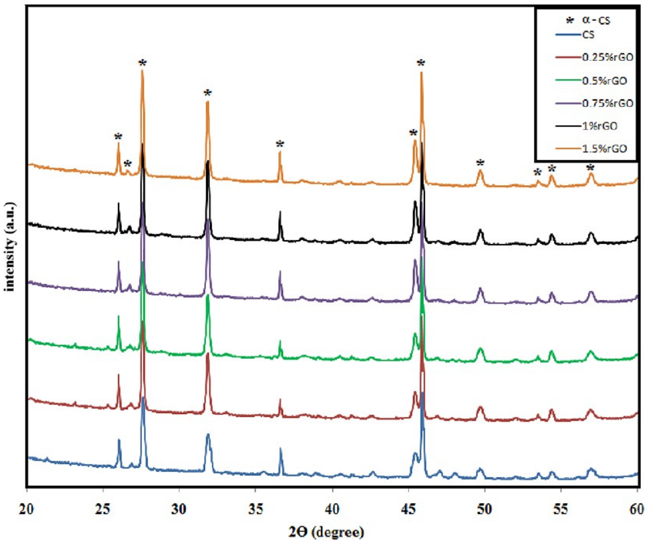

Figure 6. XRD patterns of CS−rGO composites sintered at 1150 °C by HIP.

3.2. Microstructural and Mechanical Properties of CS/rGO Composites. High densification of the composites is necessary to obtain enhanced toughness, hardness, and elastic modulus. As shown in Table 1, CS and CS/rGO have densities greater than 94%, up to 1 wt % rGO in the CS matrix, as determined using the Archimedes method. In addition, the density decreases with increasing rGO content in the composites because rGO separates the grains of the matrix, preventing pore closure.

Figure 7c,d illustrate that the pores on the surface of the CS−1.5 wt % rGO composite are open and unbent. The relative density is the lowest at 1.5 wt % rGO, at approximately 85%. This is probably because the rGO tends to be distributed in the grain boundaries of the CS matrix, which hampers the densification process.[20] Moreover, at a high concentration of rGO, pores are likely to be formed when a good bond between rGO and CS matrix is not formed, which makes it difficult to accommodate different shrinkages in the interface between rGO and CS matrix during cooling proces. In addition, overlapping of rGO exists in the sample containing 1.5 wt % rGO as is observed in Figure 7c,d, which indicate agglomeration of rGO occurs. The agglomeration of rGO significantly affects the sintered body, reducing the density and mechanical properties.[20,22] Although increasing the porosity of the CS/rGO composite might decrease its mechanical properties, these pores contribute to osteoblast ingrowth into the composite. Figure 7a,b show the fracture surfaces of

Table 1. Mechanical Properties of CS and CS/rGO Composites

sample	relative density (%)	elastic modulus (GPa)	microhardness (GPa)	nanohardness (GPa)	fracture toughness (MPa m$^{1/2}$)
CS	98 ± 0.3	76.2 ± 3.4	3.24 ± 0.17	3.55 ± 0.2	1.24 ± 0.09
CS−0.25 wt % rGO	97 ± 0.5	81.38 ± 2.8	3.84 ± 0.11	4.07 ± 0.25	1.46 ± 0.07
CS−0.5 wt % rGO	96.5 ± 0.8	97.14 ± 3.7	3.91 ± 0.06	4.2 ± 0.33	1.70 ± 0.02
CS−0.75 wt % rGO	96 ± 0.5	98.6 ± 3.9	4.57 ± 0.10	4.76 ± 0.15	2.29 ± 0.08
CS−1.0 wt % rGO	94 ± 0.7	115.72 ± 4.6	4.54 ± 0.16	4.83 ± 0.11	2.76 ± 0.07
CS−1.5 wt % rGO	85 ± 0.8	74.55 ± 2.45	2.97 ± 0.11	2.95 ± 0.3	1.83 ± 0.11

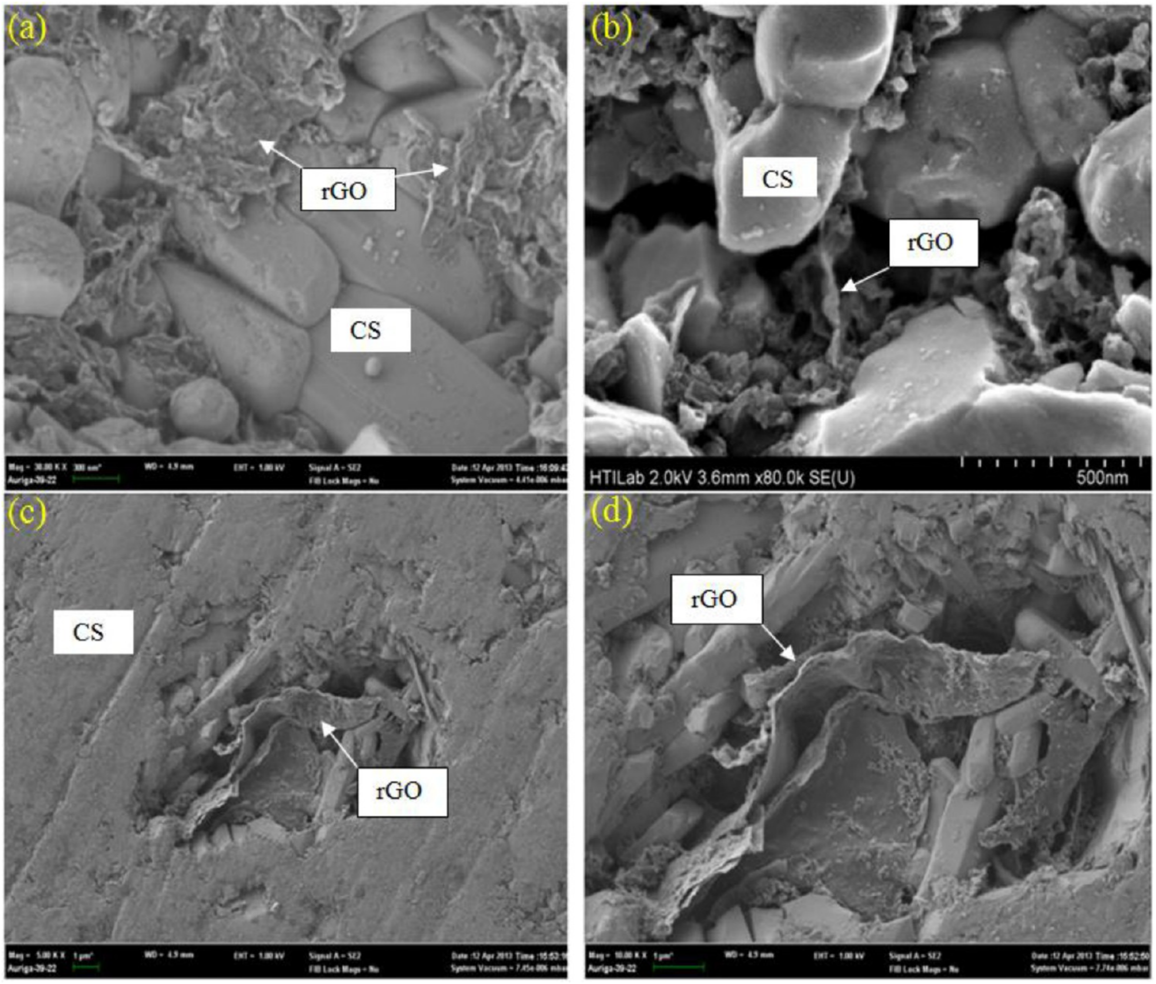

Figure 7. FESEM micrographs of CS/rGO composites after HIP consolidation. (a),(b) Fracture surface of rGO-reinforced CS composites at 1150 °C by HIP. (c),(d) Pores in the polished surface of CS−1.5 wt % rGO, with visible graphene sheets.

sintered CS/rGO pellets at 1150 °C. These highly magnified images show that many rGO pellets are well distributed in the composite matrix, indicating good dispersion of rGO.

Table 1 reports the variations in mechanical properties with the amount of rGO. Microhardness is an important mechanical property for ceramics and is critical when abrasive or grinding action is required. The Vickers hardness and nanoscale hardness for the composites containing 0.75 wt % rGO and 1 wt % rGO were ~40 and ~35% higher than those of pure CS. The absolute hardness values differ between nanoindentation and Vickers experiments due to the vast differences in applied load, tip geometry, and measurement length scale.[60] The advantage of the microindetation test is that a much larger volume is indenter and a higher volume fraction of rGO is encountered as compared to nanoindentation. The addition of rGO improves the hardness of CS up to 1 wt % rGO. The hardness is reduced at 1.5 wt % rGO because of increased porosity of the composite. As shown in Figure 7a,b, rGO is observed to wrap around CS grains. The high specific surface area of rGO can result in an increased contact area with the matrix. This could significantly increase the bonding strength between rGO and CS grains, requiring more energy to pull the nanofiller out from the CS matrix. The elastic modulus values of the HIPed pellets increased from 76.2 ± 3.4 GPa for the pure CS to 115.72 ± 4.6 GPa for the CS−1 wt % rGO but decreased again to 74.55 ± 2.45 GPa for CS−1.5 wt % rGO pellets. The increase in the elastic modulus of CS−rGO pellets is due to the high elastic modulus of graphene, the appropriate relative density of CS−rGO composites, and good bonding at the CS−rGO interface. Porosity has been reported to be a major factor governing the elastic modulus for some ceramic materials, with greater porosity correlated with a lower elastic

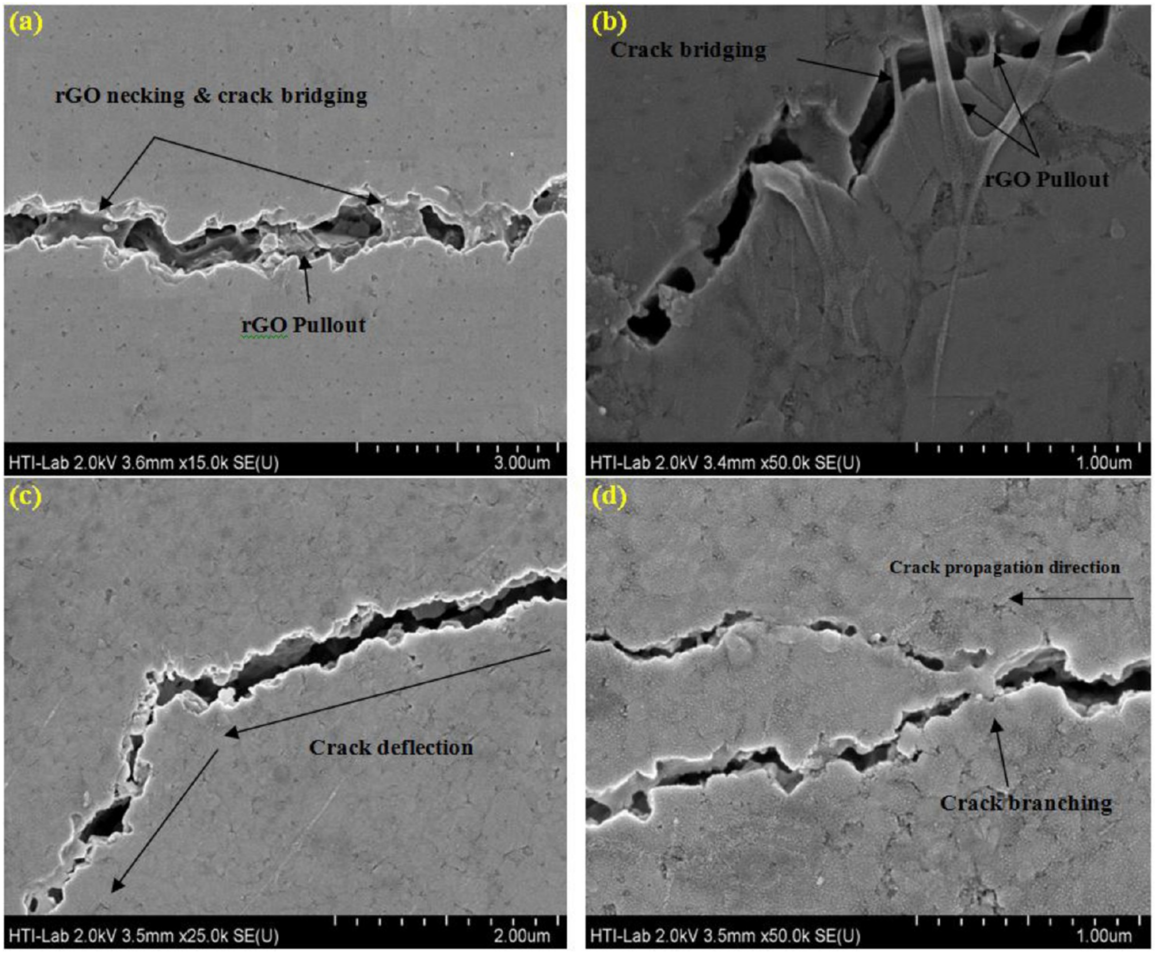

Figure 8. Toughening mechanisms in CS−rGO composites: (a),(b) crack bridging and rGO pull-out, (c) crack deflection, and (d) rGO crack branching.

modulus.[61] This explains the reduction of the elastic modulus in CS−1.5 wt % rGO pellets. The elastic modulus of human cortical bone is reported to be in the range of 15−25 GPa,[62] whereas the modulus is much higher for consolidated pure CS and our composites. A mismatch of the elastic modulus at the bone−implant interface might pose a risk of fracture or delamination of the implant.[62] Nevertheless, the osseointegration ability of CS creates strong bonding at the CS−bone interface, decreasing the chance of fracture and delamination. Likewise, an increase in the elastic modulus directly influences the improvement in the fracture toughness in ceramic-based composite systems.[63] The addition of rGO to CS results in an improvement in the indentation fracture toughness, as shown in Table 1. The fracture toughness is increased by 123% in the CS−1 wt % rGO composite. The increase in toughness correlates with increasing rGO content, but this trend does not continue for CS−1.5 wt % rGO due to the lower fracture toughness of the composite caused by the increasing porosity.[63] Four distinct rGO toughening mechanisms have been observed in CS−rGO composites, as shown in Figure 8. These mechanisms include the following: (a) crack bridging, (b) rGO pull-out, (c) crack deflection, and (d) rGO crack branching. Crack bridging is a frequently observed toughening mechanism in the CS−rGO composites. As seen in Figure 8a,b, rGO sheets can act as bridges and restrict the widening of the cracks. The rGO bridges increase the energy required to open the cracks and toughen the material. Other studies have also shown evidence of graphene bridging as an effective mechanism for the toughening of composite structures.[19,21,22,64] Pulling rGO out of the composite matrix can dissipate energy because of binding and friction, leading to toughening. Figure 8b presents FESEM images of rGO pull-out from the fracture surfaces of CS−rGO composites. Recent studies have shown that the highest fracture toughness could be obtained in composites containing graphene with a small average lateral size, as graphene with a larger lateral size causes porosity, which probably results in a weak adhesion bond of graphene/matrix and low energy dissipation during the pull-out.[65−67] As shown in Figure 8c, the resistance of rGO can be so strong that the crack seeks a lower energy path, resulting in crack deflection and energy absorption, leading to a toughening of the matrix. Crack branching of rGO can be observed in Figure 8d, which consumes more energy and leads to an increase in the resistance to crack propagation. Crack branching is a very frequently observed toughening mechanism in all studied composites containing graphene.[19,23,65] Dusza et al.[65] investigated the influence of the addition of graphene with different lateral size on the fracture toughness of graphene-reinforced Si_3N_4 composites. They found that the origin of the branching mechanism is the interaction of the propagating crack and graphene with smaller size, which was between 0.5 and 3 μm. As mentioned earlier, in our case, the average lateral size for the rGO sheets is 2.37 ± 0.65 μm. Thus, crack branching can cause an increase in the fracture toughness of CS−rGO composites.

On the basis of these observations and analysis, we can infer that rGO pull-out, crack deflection, crack branching, and crack bridging by rGO are responsible for the improved fracture toughness of CS−rGO composites.

3.3. Apatite-Forming Ability of CS/rGO Composites.

Figure 9 presents the XRD patterns of CS/rGO composites after soaking in SBF for 14 days. The intensity of the CS diffraction peaks decreased, and hydroxyapatite peaks (standard card no. JCPD 24-0033) were obvious after soaking in SBF. When the rGO content in the composite increased, most diffraction peaks of CS disappeared, and broad peaks at 2θ = 31.7°, 2θ = 49.5°, and 2θ = 53.2° and a strong peak 2θ = 26° corresponding to the (2 1 1), (2 1 3), (0 0 4), and (0 0 2) planes of hydroxyapatite (HA), respectively, became more obvious. These results suggest that more HA is formed on the surface of composites with more rGO content, and the peak shapes indicate that this HA should be nanocrystalline. Furthermore, no cristobalite or other peaks were observed in any samples soaked in SBF. FESEM micrographs of CS/rGO composites soaked in SBF for 7 and 14 days are presented in Figures 10 and 11, respectively, at both high and low magnification. The high magnification images in Figure 10 demonstrate that after soaking in SBF for 7 days, the surface microstructure varied with rGO concentration. Increasing concentrations of rGO promote the growth of nanosheet-like apatite, although pure CS ceramic exhibited worm-like crystals with the typical HA morphology. After 14 days of soaking, a densely packed HA layer covered the whole surface of the rGO containing samples, and some microcracks could also be observed on the composite surfaces due to the shrinkage and desiccation of the soaked samples in air, suggesting the formation of a thick deposit.[68,69]

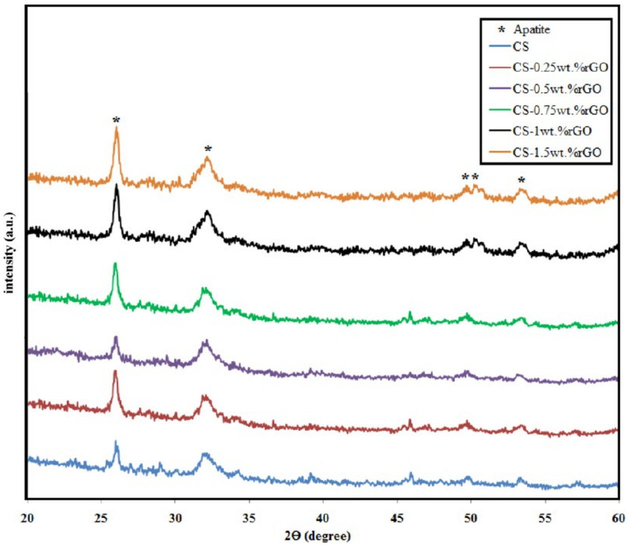

Figure 9. XRD patterns of CS−rGO composites after soaking in SBF for 14 days.

A higher-magnification examination of the samples after 14 days of soaking showed that the morphologies of the specimens were similar to those of the samples soaked for 7 days. According to the EDX spectra shown in Figure 11, the elements detected were mainly Ca and P, and no Si peaks were detected. The Ca/P molar ratio was analyzed for all the samples. The Ca/P molar ratio of the apatite formed on the pure CS and CS/rGO composites is in the range of 1.72 and 1.58, close to that of HA, which is 1.67, suggesting that apatite formed on the CS−rGO composites. These results are consistent with the results of XRD analysis and FESEM observation. Altogether, the ability to form apatite on calcium silicate ceramics has not been negatively influenced by the incorporation of reduced graphene oxide.

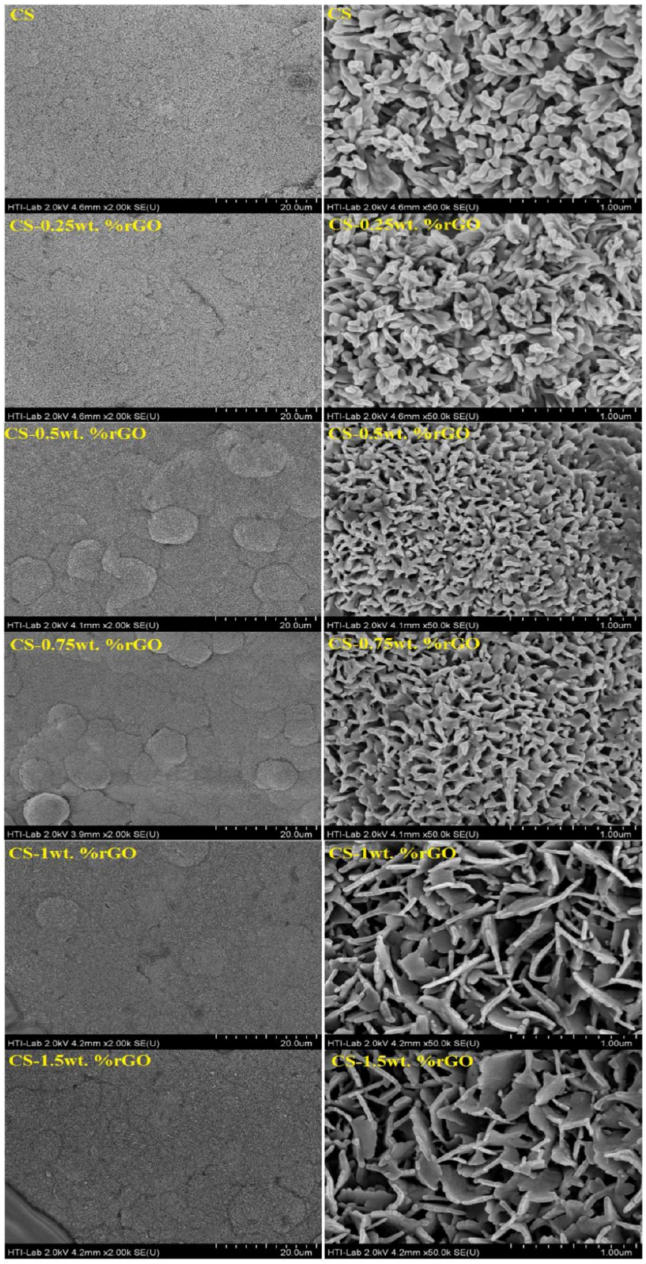

Figure 10. Low- and high-magnification FESEM images of apatite formation on CS−rGO composites immersed in SBF for 7 days.

The concentrations of Si, Ca, and P in SBF and the pH of the immersion solutions as a function of soaking time are presented in Figure 12. The concentration of Si ions increased slightly with an increasing amount of rGO in the ceramic (Figure 12b), whereas no significant differences were observed in Ca concentration between pure CS and CS/rGO composites as the rGO content was increased (Figure 12a). The P concentration continuously decreased during the soaking of the samples in SBF. As shown in Figure 12c, the P ion concentration decreases with increasing rGO content. The

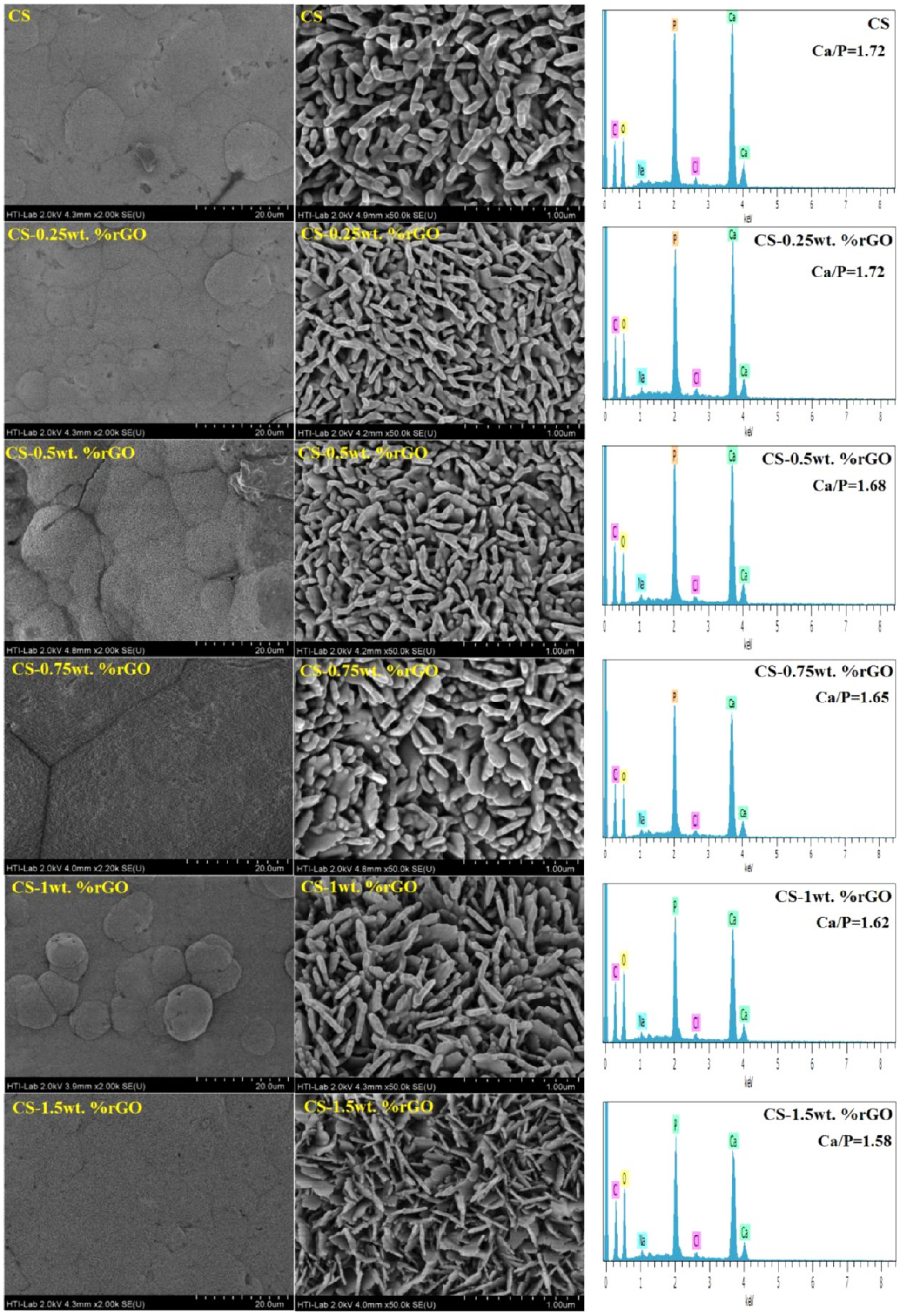

Figure 11. Low- and high-magnification FESEM images of apatite formation on CS−rGO composites immersed in SBF for 14 days.

reduced phosphate concentration can be attributed to the formation of amorphous calcium phosphate and the subsequent formation of HA by incorporating OH^- ions from the SBF, providing an indirect indication that a precipitation reaction occurred.[70] Figure 12d shows that the pH of the immersion solution increased for all samples. Previous studies have shown that the release of Ca and Si ions from CS can lead to increased pH of the SBF solution.[39,71,72] In our study, we observed that the pH of the SBF used to soak rGO-containing CS was lower than that used to soak pure CS ceramic, especially for CS/rGO composites with higher amounts of rGO. This indicates that some acidic byproducts were produced during the soaking. As discussed in FTIR results, for the rGO, the bands associated with the oxygen functional groups decrease in relation to those of GO. Nevertheless, the elimination of these bands is not complete. Furthermore, The FTIR analysis indicated that carboxyl groups and a small fraction of hydroxyl functionalities still remain in the rGO, which can react with atmospheric humidity to form acids. These functional groups may have been the cause for the lower pH upon exposure of rGO to SBF.

CS has been recommended as a material to promote bone tissue regeneration, as it could facilitate the formation of HA layers between living tissue and the implant material.[39,73] The bone-like HA plays a vital role in forming a chemical bond

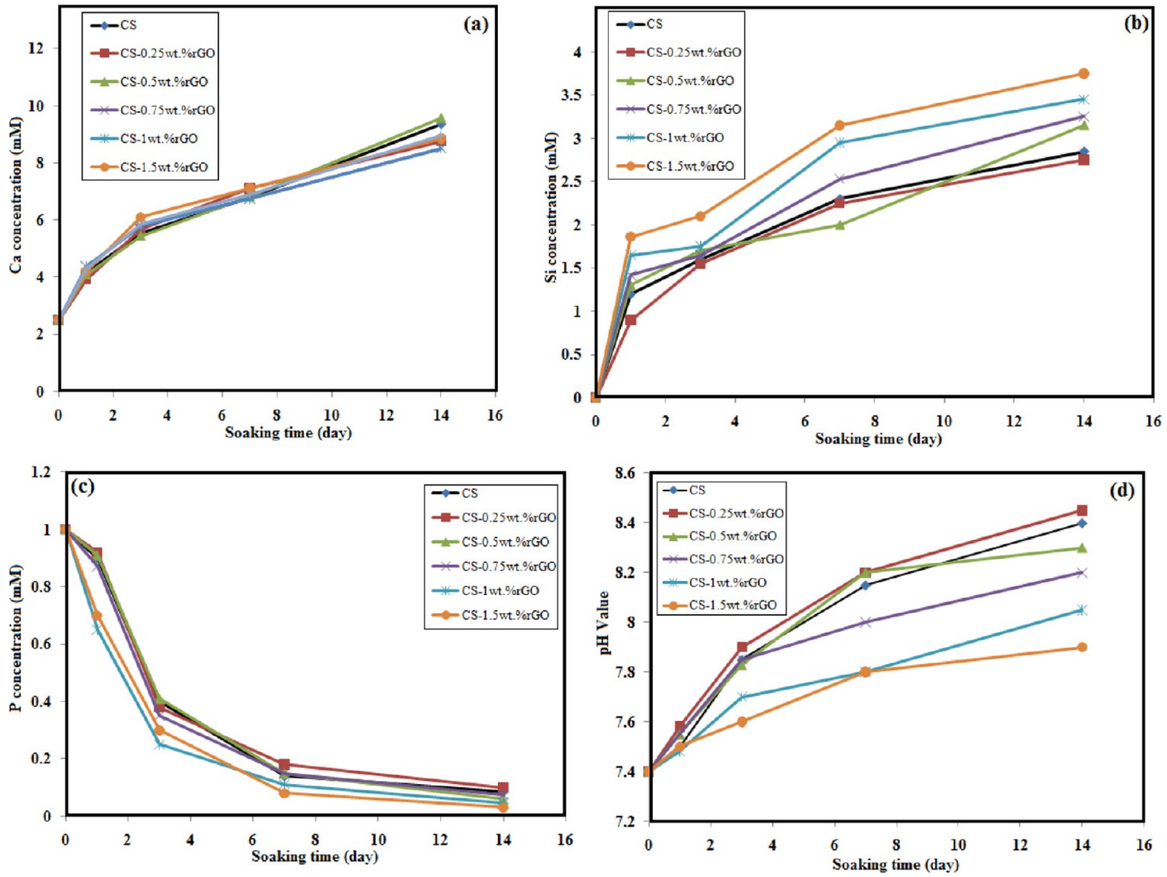

Figure 12. Effect of rGO content in CS composites on the Ca (a), Si (b), P (c) ion release, and the change in the pH value (d) in the SBF solution after soaking for various durations.

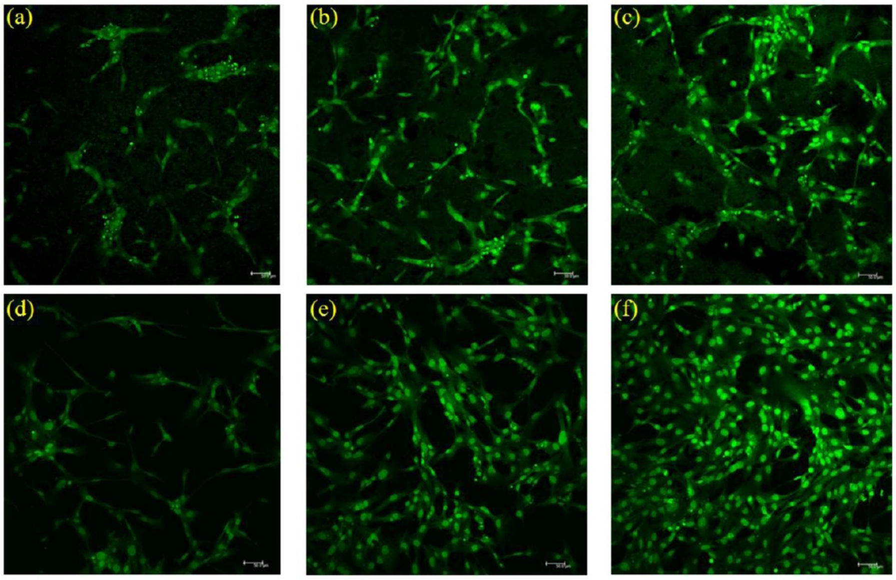

Figure 13. Confocal images of adherent hFOB cells on pure CS for 1 (a), 3 (b), and 5 (c) days and CS−1 wt % rGO composites for 1 (d), 3 (e), and 5 (f) days incubation. The scale bar represents 50 μm.

between the bioactive material and the living tissue, and the in vitro formation of bone-like HA in SBF predicts a useful bone-bonding ability.[30,73,74]

A number of groups have reported the mechanisms of HA formation on CS surfaces through in vitro incubation in SBF solution. Some reports state that an ionic interchange of Ca^{2+} for $2H^+$ occurs at the surface, resulting in the formation of an amorphous silica layer on the surface of CS, which provides favorable sites for apatite nucleation.[29,75] Additionally, the degree of supersaturation of the solution with respect to apatite increases with ion dissolution. Therefore, apatite nuclei are rapidly created on the sample surface, and they spontaneously

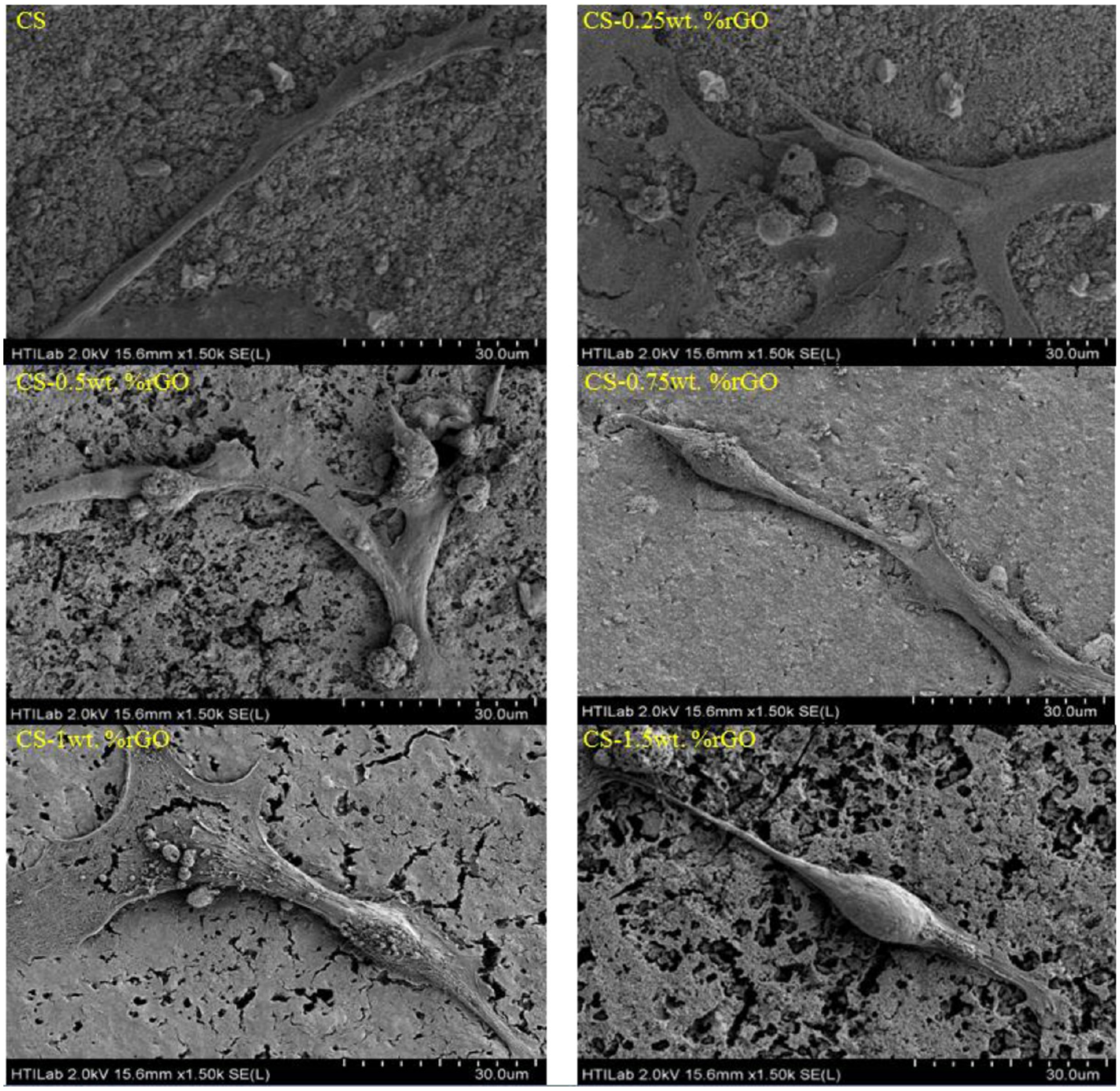

Figure 14. FESEM illustrating the morphology of hFOB cells seeded on pure CS and CS−rGO composites after 24 h.

grow by consuming calcium and phosphate ions from the surrounding fluid.[75] In the present study, although the increase in rGO content from 0 wt % to 1.5 wt % did not increase the Ca^{2+} ion concentration in the SBF, a slightly higher Si^{4+} ion concentration was observed in SBF for the composites compared to pure CS. When bone forms, the cross-linking of the collagen chain and the subsequent precipitation of HA are pH-dependent and require an optimal pH at the site of bone formation.[39] Solution pH is also a key factor affecting cell vitality.[73] Our results showed that greater amounts of rGO in CS/rGO ceramics decreased the pH of the SBF due to the exposure of rGO to the SBF. Interestingly, the HA morphology varied among different rGO-containing CS ceramics. This morphological difference of HA grown in SBF-based solutions can be attributed to changes in the ion concentrations and pH in SBF after the soaking of different rGO-containing CS ceramics. Our results showed that CS/rGO composites sintered by HIP also possessed excellent bioactivity and could develop a bone-like HA layer on their surface when soaked in SBF. Moreover, the ability to form apatite on CS ceramics was not influenced by increases in rGO content up to 1.5 wt %, as illustrated by the intensity of the HA peaks on XRD and FESEM. In addition, these results suggest that CS/rGO ceramics have potential applications for in vitro bone cell culture.

3.4. In Vitro Biocompatibility of CS/rGO Composites with Osteoblasts. The CS/rGO composite is intended for use in orthopedic implant applications. Therefore, the orthopedic implant should promote cellular adhesion, proliferation, and differentiation. Osteoblasts are able to attach to the orthopedic implant surface. They actively participate in new bone formation by first forming a collagen matrix and then assisting in the deposition of apatite crystal on that matrix. Thus, the growth and proliferation of osteoblast cells on an implant surface plays a crucial role in osseointegration and in determining the lifetime of an implant.[60,62] Thus, the effect of rGO on the growth and proliferation of human osteoblast cells (hFOB) was assessed qualitatively by observing the population of osteoblast cells on the surface after 1, 3, and 5 days of culture.

Figure 13 presents confocal laser scanning microscopy (CLSM) images of hFOB cells cultured on the surface of pure CS and CS−1.0 wt % rGO pellets. The cells exhibit a typical lens shape, suggesting normal cell growth. The osteoblast population clearly increases from 1 to 5 days on both surfaces. This observation indicates that CS and CS/rGO surfaces are suitable for osteoblast cell proliferation. Interestingly, more osteoblast cells are attached to the CS/rGO surface than the pure CS surface after 3 and 5 days of culture. Figure 14 shows the osteoblast cell morphology on pure CS and CS/rGO composites after 24 h of culture. In general, the hFOB cells on all the CS/rGO composites are globular, flat, and actively spreading with a number of filopodia protrusions, an indication of a normal cell attachment and growth process.[76]

Extracellular matrix (ECM) was secreted by the seeded hFOB cells, and the cells merged on the surface of CS/rGO composites to form cell layers. Merging induced the formation of a rich ECM, indicative of high cell activity on the CS/rGO composites. Bone is produced by the mineralization of an organic matrix (largely collagen) through the nucleation and growth of a mineral similar to HA.[30] Thus, the presence of calcium phosphate in the ECM acts as a key factor in the regulation of bone remodelling and cartilage.[76] Mineralization of hFOB cultured on CS−1 wt % rGO composite after 3 days cell culture was observed by FESEM, as shown in Figure 15b. In the present study, the EDX pattern of hFOB cells on the CS−1 wt % rGO indicated the formation of a calcium phosphate based on the preponderance of Ca and P elements as presented in Figure 15c. In addition, the Ca/P molar ratio on the surface of merging cell layers was 1.64 and was approximately equal to the 1.67 ratio of HA, suggesting that the calcium phosphate formed in the ECM mainly consisted of apatite, which is the major inorganic composition of bones and cartilages. Therefore, it is plausible to suggest that the CS/rGO composite is expected to be suitable for bone regeneration.

Cell viability was studied with an MTT assay by seeding osteoblasts onto the rGO-containing CS for 1, 3, and 5 days, and the results are summarized in Figure 16. The MTT activity increased with incubation time, indicating that proliferation proceeded on all specimens. In other words, rGO addition did not exhibit any obvious effects on cell proliferation. Interestingly, the number of cultured cells increased significantly with increasing rGO concentration. As an increase in cell number is preferred over an increase in osteoblast activity, the initial proliferation and recruitment of cells to the implant surface is important. Our finding is consistent with recent reports by other researchers that incorporation of graphene or rGO into silica, HA, and chitosan leads to better adherence and stimulated proliferation of human osteoblasts and mesenchymal stromal cells than on pure silica, HA, and chitosan.[21,77,78] To better understand the effect of rGO on the behavior of the hFOB cells, osteoblast differentiation is one of the most important steps in overall cellular activity and thus bone-formation ability. Thus, the effects of rGO on osteoblast differentiation were evaluated using an alkaline phosphate activity (ALP) assay, which is an early marker of osteoblast differentiation. Figure 17 shows the proliferation and ALP activity of the hFOB cells cultured on pure CS for 7 days. The cells cultured for 7 days on the pure CS and CS/rGO composites exhibited significantly higher ALP activity than the blank well plate. The ALP activity of the cells on the composites markedly increased with increasing rGO content in the composites. The ALP expression level on the CS−1 wt % rGO composite was approximately 1.5 times higher than that on the pure CS ceramic. The cell attachment, proliferation, and differentiation data for pure CS and CS/rGO composites demonstrate a high degree of CS/rGO composite−osteoblast interaction and indicate that this is a successful in vitro model to study bone cell−biomaterial interactions. Previous studies

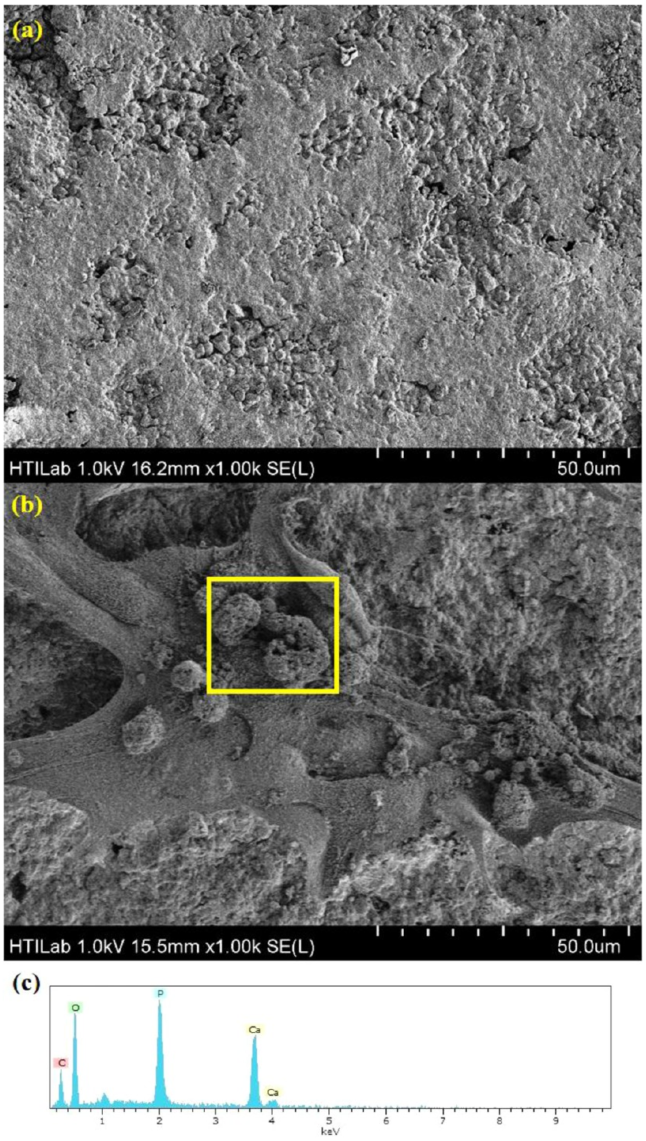

Figure 15. (a) CS−1 wt % rGO composite without cells. (b) hFOB cells grown on CS−1 wt % rGO composite after 3days. (c) EDX spectra of the hFOB cells in the boxed region that is showing a significant presence of P and Ca on the CS/rGO CS−1 wt % rGO composite after 3 days of seeding.

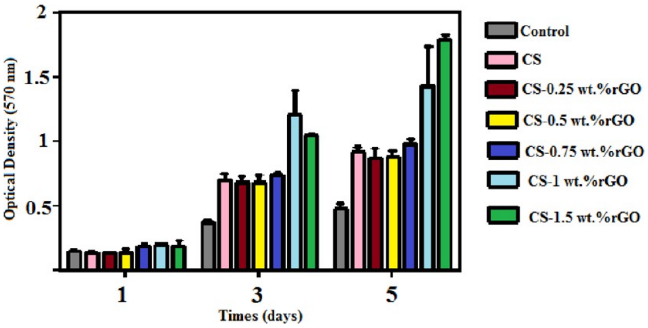

Figure 16. Cell culture results for the CS−rGO pellets. The hFOB cells cultured on the sample surfaces exhibit enhanced proliferation with an increased content of rGO in the composites.

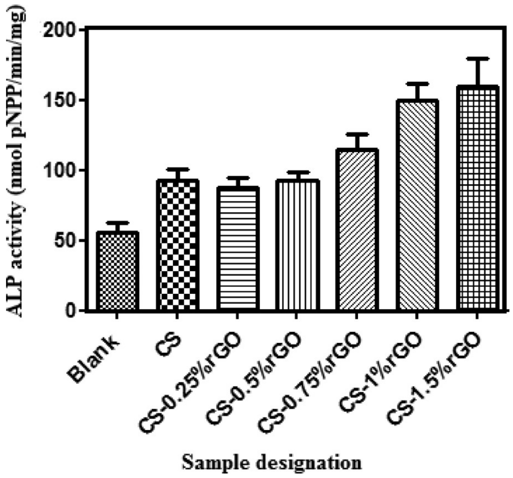

Figure 17. ALP activity of hFOB cells after cultivation on different CS−rGO composites for 7 days.

found that the Ca and Si ions released from materials stimulate osteoblast differentiation, gene expression, and proliferation, which can be regarded as evaluation criteria for bioactivity.[30,79] Furthermore, the ALP activity and osteocalcin levels increased when Si was exposed to human osteoblasts.[38] Our results showed that Si concentrations in SBF increased with increasing rGO content, whereas the amount of Ca ion released was approximately equal to that of pure CS. Note that the pH value has multiple effects on osteoblast metabolism and function, with a pH value of 7.6 increasing osteoblastic collagen synthesis.[38,80] Our results indicated a smaller increase in the pH of SBF due to increased rGO content in the CS ceramic, which can be desirable for cell growth. Moreover, recent reports indicate other influences of graphene on the cell viability, proliferation, and gene expression of osteoblasts. Chen et al.[81] reported that graphene can support induced pluripotent stem cell (iPSC) culture and allow for spontaneous differentiation. The graphene surface led to distinct cell proliferation and differentiation characteristics.

Their data demonstrated that the surface properties of graphene governed the iPSC behavior and indicated the potential of graphene-based materials as a platform for iPSC culture and other applications. Kalbacova et al.[77] indicated that the electrical conductivity of graphene is particularly important because electricity, cocktails of growth factors, and substrate properties are able to stimulate cell growth and differentiation. Additionally, a very recent study suggested that the cell viability of rGO depended on the lateral size of the sheets.[28,82] Taken together, the results of the present work demonstrate that rGO possesses sufficient biocompatibility for use as a biomaterial and that the addition of rGO into the CS matrix is remarkably effective in improving the cellular response to the CS ceramic.

4. CONCLUSIONS

In summary, we used a hydrothermal processing method to synthesize calcium silicate (Xonotlite phase)-reduced graphene oxide composite powders. This method produced CS nanowires in the Xonotlite phase with approximate diameters of 10−30 nm and lengths up to several micrometers that nucleate on and grow along graphene sheets. After densification at 1150 °C by HIP, we obtained direct evidence of rGO in the composites using Raman spectroscopy, FTIR, and FESEM. Most interestingly, we observed that the CS−1.0 wt % rGO composite displays improved hardness, elastic modulus, and fracture toughness compared to pure CS. The main toughening mechanisms are crack deflection, crack branching, crack bridging, and graphene sheet pull-out on the fracture surface. Moreover, the addition of rGO did not affect the ability to form apatite on CS ceramics. Interestingly, the introduction of rGO into the CS matrix stimulated hFOB proliferation and significantly increased the ALP activity of hFOB cells compared with pure CS ceramics in 7 day experiments. Our results suggest that the addition of rGO into the CS resulted in composites with improved mechanical properties and that the composite with 1 wt % rGO content might be a promising bone implant material due to its improved mechanical and biological properties compared with pure CS ceramics.

■ AUTHOR INFORMATION

Corresponding Authors

*E-mail: (S.F.S.S.) f.shirazi@siswa.um.edu.my. Fax: +60 03 79675317. Tel.: +60 142646276.
*E-mail: (H.S.C.M.) h.metselaar@um.edu.my.

Notes

The authors declare no competing financial interest.

■ ACKNOWLEDGMENTS

This work was financially supported by the Ministry of High Education (MOHE) of Malaysia through grant number UM.C/HIR/MOHE/ENG/10 D000010-16001 and by a national grant from the Malaysian FRGS (FP007/2013A). The authors thank the Bright Sparks Unit (University of Malaya) for additional financial support.

■ REFERENCES

(1) Ferrari, A. C.; Basko, D. M. *Nat. Nanotechnol.* **2013**, *8*, 235−246.
(2) Geim, A. K.; Novoselov, K. S. *Nat. Mater.* **2007**, *6*, 183−191.
(3) Mehrali, M.; Latibari, S. T.; Mehrali, M.; Metselaar, H. S. C.; Silakhori, M. *Energy Convers. Manage.* **2013**, *67*, 275−282.
(4) Xu, Z. P.; Buehler, M. J. *ACS Nano* **2010**, *4*, 3869−3876.
(5) Akhavan, O.; Ghaderi, E. *ACS Nano* **2010**, *4*, 5731−5736.
(6) Tang, J.; Chen, Q.; Xu, L. G.; Zhang, S.; Feng, L. Z.; Cheng, L.; Xu, H.; Liu, Z.; Peng, R. *ACS Appl. Mater. Interfaces* **2013**, *5*, 3867−3874.
(7) Akhavan, O.; Ghaderi, E.; Rahighi, R. *ACS Nano* **2012**, *6*, 2904−2916.
(8) Zhang, L. M.; Xia, J. G.; Zhao, Q. H.; Liu, L. W.; Zhang, Z. J. *Small* **2010**, *6*, 537−544.
(9) Peng, C.; Hu, W. B.; Zhou, Y. T.; Fan, C. H.; Huang, Q. *Small* **2010**, *6*, 1686−1692.
(10) Robinson, J. T.; Tabakman, S. M.; Liang, Y. Y.; Wang, H. L.; Casalongue, H. S.; Vinh, D.; Dai, H. J. *J. Eur. Ceram. Soc.* **2011**, *133*, 6825−6831.
(11) Akhavan, O.; Choobtashani, M.; Ghaderi, E. *J. Phys. Chem. C* **2012**, *116*, 9653−9659.
(12) Fan, Z. J.; Wang, J. Q.; Wang, Z. F.; Ran, H. Q.; Li, Y.; Niu, L. Y.; Gong, P. W.; Liu, B.; Yang, S. R. *Carbon* **2014**, *66*, 407−416.
(13) Zhou, K.; Thouas, G. A.; Bernard, C. C.; Nisbet, D. R.; Finkelstein, D. I.; Li, D.; Forsythe, J. S. *ACS Appl. Mater. Interfaces* **2012**, *4*, 4524−4531.
(14) Liao, K. H.; Lin, Y. S.; Macosko, C. W.; Haynes, C. L. *ACS Appl. Mater. Interfaces* **2011**, *3*, 2607−2615.
(15) Castelain, M.; Martinez, G.; Marco, C.; Ellis, G.; Salavagione, H. J. *Macromolecules* **2013**, *46*, 8980−8987.
(16) Ramanathan, T.; Abdala, A. A.; Stankovich, S.; Dikin, D. A.; Herrera-Alonso, M.; Piner, R. D.; Adamson, D. H.; Schniepp, H. C.; Chen, X.; Ruoff, R. S.; Nguyen, S. T.; Aksay, I. A.; Prud'homme, R. K.; Brinson, L. C. *Nat. Nanotechnol.* **2008**, *3*, 327−331.

(17) Walker, L. S.; Marotto, V. R.; Rafiee, M. A.; Koratkar, N.; Corral, E. L. *ACS Nano* **2011**, *5*, 3182−3190.

(18) Ramirez, C.; Miranzo, P.; Belmonte, M.; Osendi, M. I.; Poza, P.; Vega-Diaz, S. M.; Terrones, M. *J. Eur. Ceram. Soc.* **2014**, *34*, 161−169.

(19) Liu, J.; Yan, H. X.; Reece, M. J.; Jiang, K. *J. Eur. Ceram. Soc.* **2012**, *32*, 4185−4193.

(20) Liu, J.; Yan, H.; Jiang, K. *Ceram. Int.* **2013**, *39*, 6215−6221.

(21) Liu, Y.; Huang, J.; Li, H. *J. Mat. Chem. B* **2013**, *1*, 1826−1834.

(22) Zhang, L.; Liu, W.; Yue, C.; Zhang, T.; Li, P.; Xing, Z.; Chen, Y. *Carbon* **2013**, *61*, 105−115.

(23) Zhao, Y.; Sun, K.-N.; Wang, W.-L.; Wang, Y.-X.; Sun, X.-L.; Liang, Y.-J.; Sun, X.-N.; Chui, P.-F. *Ceram. Int.* **2013**, *39* (7), 7627−7634.

(24) Li, M.; Wang, Y.; Liu, Q.; Li, Q.; Cheng, Y.; Zheng, Y.; Xi, T.; Wei, S. *J. Mater. Chem. B* **2013**, *1*, 475−484.

(25) He, Q. Y.; Sudibya, H. G.; Yin, Z. Y.; Wu, S. X.; Li, H.; Boey, F.; Huang, W.; Chen, P.; Zhang, H. *ACS Nano* **2010**, *4*, 3201−3208.

(26) Hu, C. F.; Liu, Y. L.; Qin, J. L.; Nie, G. T.; Lei, B. F.; Xiao, Y.; Zheng, M. T.; Rong, J. H. *ACS Appl. Mater. Interfaces* **2013**, *5*, 4760−4768.

(27) Agarwal, S.; Zhou, X. Z.; Ye, F.; He, Q. Y.; Chen, G. C. K.; Soo, J.; Boey, F.; Zhang, H.; Chen, P. *Langmuir* **2010**, *26*, 2244−2247.

(28) Akhavan, O.; Ghaderi, E.; Akhavan, A. *Biomaterials* **2012**, *33*, 8017−8025.

(29) Liu, X. Y.; Ding, C. X.; Wang, Z. Y. *Biomaterials* **2001**, *22*, 2007−2012.

(30) Gandolfi, M. G.; Ciapetti, G.; Taddei, P.; Perut, F.; Tinti, A.; Cardoso, M. V.; Van Meerbeek, B.; Prati, C. *Dent. Mater.* **2010**, *26*, 974−992.

(31) Ni, S. Y.; Chang, J.; Chou, L. *J. Biomed. Mater. Res., Part A* **2006**, *76A*, 196−205.

(32) Ni, S. Y.; Chang, J.; Chou, L.; Zhai, W. Y. *J. Biomed. Mater. Res., Part B* **2007**, *80B*, 174−183.

(33) Magallanes-Perdomo, M.; De Aza, A. H.; Mateus, A. Y.; Teixeira, S.; Monteiro, F. J.; De Aza, S.; Pena, P. *Acta Biomater.* **2010**, *6*, 2254−2263.

(34) Lu, B. Q.; Zhu, Y. J.; Ao, H. Y.; Qi, C.; Chen, F. *ACS Appl. Mater. Interfaces* **2012**, *4*, 6968−6973.

(35) Lin, K. L.; Zhai, W. Y.; Ni, S. Y.; Chang, J.; Zeng, Y.; Qian, W. J. *Ceram. Int.* **2005**, *31*, 323−326.

(36) Long, L. H.; Zhang, F. M.; Chen, L.; Chen, L. D.; Chang, J. *J. Eur. Ceram. Soc.* **2008**, *28*, 2883−2887.

(37) Zhao, S. J.; Wang, L. J.; Jiang, W.; Zhang, J. F.; Chen, L. D. *Mater. Trans.* **2008**, *49*, 2310−2314.

(38) Wu, C. T.; Ramaswamy, Y.; Soeparto, A.; Zreiqat, H. *J. Biomed. Mater. Res., Part A* **2008**, *86A*, 402−410.

(39) Wu, C. T.; Ramaswamy, Y.; Kwik, D.; Zreiqat, H. *Biomaterials* **2007**, *28*, 3171−3181.

(40) Shirazi, F. S.; Mehrali, M.; Ataollahi Oshkour, A.; Cornelis Metselaar, H. S.; Kadri, N. A.; Abu Osman, N. A. *Int. J. Appl. Ceram. Technol.* **2013**, No. 10.1111/ijac.12151.

(41) Lin, K. L.; Chang, J.; Cheng, R. M. *Acta Biomater.* **2007**, *3*, 271−276.

(42) Li, X. K.; Chang, J. *J. Mater. Sci.* **2006**, *41*, 4944−4947.

(43) Pei, L. Z.; Yang, L. J.; Yang, Y.; Fan, C. G.; Yin, W. Y.; Chen, J.; Zhang, Q. F. *Mater. Charact.* **2010**, *61*, 1281−1285.

(44) Lin, K. L.; Chang, J.; Liu, X. G.; Ning, C. Q. *Int. J. Appl. Ceram. Technol.* **2010**, *7*, 178−183.

(45) Lim, H. N.; Huang, N. M.; Lim, S. S.; Harrison, I.; Chia, C. H. *Int. J. Nanomed.* **2011**, *6*, 1817−1823.

(46) Pattanayak, D. K.; Prasad, R. C.; Rao, B. T.; Mohan, T. R. R. *J. Am. Ceram. Soc.* **2006**, *89*, 2172−2176.

(47) Askari, E.; Mehrali, M.; Metselaar, I.; Kadri, N. A.; Rahman, M. M. *J. Mech. Behav. Biomed. Mater.* **2012**, *12*, 144−150.

(48) Kokubo, T.; Takadama, H. *Biomaterials* **2006**, *27*, 2907−2915.

(49) Marlinda, A. R.; Huang, N. M.; Muhamad, M. R.; An'amt, M. N.; Chang, B. Y. S.; Yusoff, N.; Harrison, I.; Lim, H. N.; Chia, C. H.; Kumar, S. V. *Mater. Lett.* **2012**, *80*, 9−12.

(50) Mehrali, M.; Latibari, S. T.; Mehrali, M.; Indra Mahlia, T. M.; Cornelis Metselaar, H. S. *Energy* **2013**, *58*, 628−634.

(51) Sookhakian, M.; Amin, Y. M.; Basirun, W. J. *Appl. Surf. Sci.* **2013**, *283*, 668−677.

(52) Muruganandham, M.; Amutha, R.; Sillanpaa, M. *ACS Appl. Mater. Interfaces* **2010**, *2*, 1817−1823.

(53) Lin, K. L.; Chang, J.; Chen, G. F.; Ruan, M. L.; Ning, C. Q. *J. Cryst. Growth* **2007**, *300*, 267−271.

(54) Wang, D. W.; Wu, K. H.; Gentle, I. R.; Lu, G. Q. *Carbon* **2012**, *50*, 3333−3341.

(55) Mostafa, N. Y.; Shaltout, A. A.; Omar, H.; Abo-El-Enein, S. A. *J. Alloy. Compd* **2009**, *467*, 332−337.

(56) Zeng, H. D.; Cao, Y.; Xie, S. F.; Yang, J. H.; Tang, Z. H.; Wang, X. Y.; Sun, L. Y. *Nanoscale Res. Lett.* **2013**, 8.

(57) Garbev, K.; Stemmermann, P.; Black, L.; Breen, C.; Yarwood, J.; Gasharova, B. *J. Am. Ceram. Soc.* **2007**, *90*, 900−907.

(58) Nieto, A.; Lahiri, D.; Agarwal, A. *Carbon* **2012**, *50*, 4068−4077.

(59) Osticioli, I.; Mendes, N. F. C.; Nevin, A.; Gil, F. R. C.; Becucci, M.; Castellucci, E. *Spectrochim. Acta, Part A* **2009**, *73*, 525−531.

(60) Lahiri, D.; Singh, V.; Benaduce, A. P.; Seal, S.; Kos, L.; Agarwal, A. *J. Mech. Behav. Biomed. Mater.* **2011**, *4*, 44−56.

(61) Zhao, X. J.; Chen, D. L.; Ru, H. Q.; Zhang, N. *J. Eur. Ceram. Soc.* **2011**, *31*, 883−892.

(62) Mehrali, M.; Shirazi, F. S.; Mehrali, M.; Metselaar, H. S. C.; Kadri, N. A. B.; Osman, N. A. A. *J. Biomed. Mater. Res. Part A* **2013**, *101*, 3046−3057.

(63) Lahiri, D.; Ghosh, S.; Agarwal, A. *Mater. Sci. Eng., C* **2012**, *32*, 1727−1758.

(64) Nieto, A.; Lahiri, D.; Agarwal, A. *Mater. Sci. Eng., A* **2013**, *582*, 338−346.

(65) Dusza, J.; Morgiel, J.; Duszova, A.; Kvetkova, L.; Nosko, M.; Kun, P.; Balazsi, C. *J. Eur. Ceram. Soc.* **2012**, *32*, 3389−3397.

(66) Kvetkova, L.; Duszova, A.; Hvizdos, P.; Dusza, J.; Kun, P.; Balazsi, C. *Scr. Mater.* **2012**, *66*, 793−796.

(67) Ramirez, C.; Miranzo, P.; Belmonte, M.; Osendi, M. I.; Poza, P.; Vega-Diaz, S. M.; Terrones, M. *J. Eur. Ceram. Soc.* **2014**, *34*, 161−169.

(68) Ni, S. Y.; Chang, J.; Chou, L. *J. Mater. Sci.: Mater. Med.* **2008**, *19*, 359−367.

(69) Zhong, H. B.; Wang, L. J.; Fan, Y. C.; He, L. F.; Lin, K. L.; Jiang, W.; Chang, J.; Chen, L. D. *Ceram. Int.* **2011**, *37*, 2459−2465.

(70) Wei, J.; Heo, S. J.; Li, C. S.; Kim, D. H.; Kim, S. E.; Hyun, Y. T.; Shin, J. W.; Shin, J. W. *Biomed. Mater. Res. Part A* **2009**, *90A*, 702−712.

(71) Shen, Y. H.; Liu, W. C.; Lin, K. L.; Pan, H. B.; Darvell, B. W.; Peng, S. L.; Wen, C. Y.; Deng, L. F.; Lu, W. W.; Chang, J. A. *Langmuir* **2011**, *27*, 2701−2708.

(72) Shirazi, F. S.; Moghaddam, E.; Mehrali, M.; Oshkour, A. A.; Metselaar, H. S. C.; Kadri, N. A.; Zandi, K.; Abu, N. A. *J. Biomed. Mater. Res., Part A* **2014**, DOI: 10.1002/jbm.a.35074.

(73) Pan, H. B.; Zhao, X. L.; Darvell, B. W.; Lu, W. W. *Acta Biomater.* **2010**, *6*, 4181−4188.

(74) Kaur, G.; Pandey, O. P.; Singh, K.; Homa, D.; Scott, B.; Pickrell, G. *J. Biomed. Mater. Res. Part A* **2013**, DOI: 10.1002/jbm.a.34690.

(75) Liu, X. Y.; Ding, C. X.; Chu, P. K. *Biomaterials* **2004**, *25*, 1755−1761.

(76) Kumar, A.; Webster, T. J.; Biswas, K.; Basu, B. *J. Biomed. Mater. Res. Part A* **2013**, *101*, 2925−2938.

(77) Kalbacova, M.; Broz, A.; Kong, J.; Kalbac, M. *Carbon* **2010**, *48*, 4323−4329.

(78) Fan, H. L.; Wang, L. L.; Zhao, K. K.; Li, N.; Shi, Z. J.; Ge, Z. G.; Jin, Z. X. *Biomacromolecules* **2010**, *11*, 2345−2351.

(79) Xynos, I. D.; Edgar, A. J.; Buttery, L. D. K.; Hench, L. L.; Polak, J. M. *Biochem. Biophys. Res. Commun.* **2000**, *276*, 461−465.

(80) Silver, I. A.; Deas, J.; Erecinska, M. *Biomaterials* **2001**, *22*, 175−185.

(81) Chen, G. Y.; Pang, D. W. P.; Hwang, S. M.; Tuan, H. Y.; Hu, Y. C. *Biomaterials* **2012**, *33*, 418−427.

(82) Zhang, H.; Peng, C.; Yang, J. Z.; Lv, M.; Liu, R.; He, D. N.; Fan, C. H.; Huang, Q. *ACS Appl. Mater. Interfaces* **2013**, *5*, 1761−1767.